A complex-scaled boundary integral equation for the embedded eigenvalues and complex resonances of the Neumann-Poincaré operator on domains with corners

Luiz Maltez Faria, Florian Monteghetti

A complex-scaled boundary integral equation for the embedded eigenvalues and complex resonances of the Neumann-Poincaré operator on domains with corners

Luiz M. Faria[a], Florian Monteghetti[b]

[a]*POEMS, CNRS, INRIA, ENSTA Paris, Institut Polytechnique de Paris, Palaiseau, 91120, France*
[b]*Aix Marseille Univ, CNRS, I2M, Marseille, France, Marseille, 13331, France*

Abstract

The adjoint of the harmonic double-layer operator, also known as the Neumann-Poincaré (NP) operator, is a boundary integral operator whose real eigenvalues are associated with surface modes that find applications in e.g. photonics. On 2D domains with corners, the NP operator looses its compactness, as each corner induces a bounded interval of essential spectrum, and can exhibit both embedded eigenvalues and complex resonances. This work introduces a non-self-adjoint boundary integral operator whose discrete spectrum contains both embedded eigenvalues and complex resonances of the NP operator. This operator is obtained using a Green's function that is complex-scaled at each corner of the boundary. Numerical experiments using a Nyström discretization on a graded mesh demonstrates the accuracy of the method and its advantage over a 2D finite element discretization implementing the same complex scaling technique.

Keywords: Neumann-Poincaré operator, Layer potential, Embedded eigenvalue, Complex resonance, Complex scaling, Perfectly Matched Layer

1. Introduction

Let $\Omega \subset \mathbb{R}^2$ be an open bounded set whose boundary is C^2 except for a finite number of straight corners, as illustrated in Figure 1 and made precise below.

Assumption 1. *The set $\Omega \subset \mathbb{R}^2$ is open, bounded, connected, with a Lipschitz boundary Γ. There is a radius $R > 0$, boundary points $\boldsymbol{x}_c^k \in \partial\Omega$, angles $\phi_k \in (0, 2\pi)\backslash\{\pi\}$, and rotation matrices Q_k, such that*

1. *Ω has a boundary of class C^2 everywhere except at $(\boldsymbol{x}_c^k)_{k\in[\![1,N_c]\!]}$.*
2. *For any $k \in [\![1, N_c]\!]$,*

$$\Omega \cap B(\boldsymbol{x}_c^k, R) = \left\{\boldsymbol{x}_c^k + Q_k[r\cos\theta, r\sin\theta] \,|\, r \in [0, R),\ \theta \in (-\phi_k/2, \phi_k/2)\right\}.$$

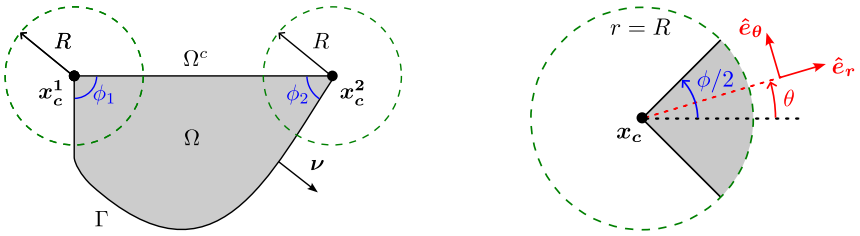

(a) Set with C^2 boundary except for straight corners.

(b) Polar coordinates centered at a corner.

Figure 1: Notation.

We define the *Neumann-Poincaré* (NP) operator as[1]

$$K^\star\sigma(\boldsymbol{x}) \coloneqq \mathrm{pv}\int_\Gamma \partial_{\nu(\boldsymbol{x})}G(\boldsymbol{x},\boldsymbol{y})\sigma(\boldsymbol{y})\,\mathrm{d}s(\boldsymbol{y}) \quad (\boldsymbol{x}\in\Gamma), \tag{1}$$

where pv denotes the Cauchy principal value, $\boldsymbol{\nu}$ is the unit normal vector that points towards $\Omega^c \coloneqq \mathbb{R}^2\backslash\overline{\Omega}$, and G is the free space Green's function of $-\Delta$:

$$G(\boldsymbol{x},\boldsymbol{y}) \coloneqq -\frac{1}{2\pi}\ln|\boldsymbol{x}-\boldsymbol{y}|,\ \partial_{\nu(\boldsymbol{x})}G(\boldsymbol{x},\boldsymbol{y}) = -\frac{1}{2\pi}\frac{(\boldsymbol{x}-\boldsymbol{y})\cdot\boldsymbol{\nu}(x)}{|\boldsymbol{x}-\boldsymbol{y}|^2} \quad (\boldsymbol{x}\neq\boldsymbol{y}). \tag{2}$$

Throughout this work, we consider $K^\star$ and its adjoint as bounded linear maps [6, 7, 8]

$$K^\star \in \mathcal{B}(H^{-1/2}(\Gamma), H^{-1/2}(\Gamma)),\ K \in \mathcal{B}(H^{1/2}(\Gamma), H^{1/2}(\Gamma)),$$

where the adjoint operator is explicitly given by

$$K\sigma(\boldsymbol{x}) \coloneqq \mathrm{pv}\int_\Gamma \partial_{\nu(\boldsymbol{y})}G(\boldsymbol{x},\boldsymbol{y})\sigma(\boldsymbol{y})\,\mathrm{d}s(\boldsymbol{y}) \quad (\boldsymbol{x}\in\Gamma). \tag{3}$$

Our interest lies in the following boundary integral (BI) eigenvalue problem.

Definition 2 (NP Eigenvalue Problem)**.** Find $(\sigma,\lambda)\in H^{-1/2}(\Gamma)\times(-1/2,1/2)$, $\sigma\neq 0$, such that

$$K^\star\sigma = \lambda\,\sigma. \tag{4}$$

This eigenvalue problem is known to exhibit somewhat exotic features when $N_c \neq 0$:

1. Each of the N_c corners in Γ induces an interval of essential spectrum associated with strongly-oscillating corner singularities.
2. Some eigenvalues can be embedded in the essential spectrum.
3. There can be *complex resonances* [9], i.e. complex singularities of the meromorphic continuation of $\lambda\mapsto(K^\star-\lambda)^{-1}$ across the essential spectrum.

The objective of this work is to compute both embedded eigenvalues and complex resonances of K; the challenge lies in the fact that a discretization of (4) leads to an eigenvalue problem with only real eigenvalues, and which converges only at isolated eigenvalues. Our contribution

[1] Common alternative definitions include $-K^\star$ [1, (1.1)] [2, (1.2)] and $2\,K$ [3, (2.77)] [4, (5)] [5, (2)].

is the construction of a non-self-adjoint BI operator $K_\alpha^\star$ whose *discrete* spectrum includes the embedded eigenvalues and complex resonances of K; we demonstrate its usefulness using a Nyström discretization on a graded mesh.

Our strategy to build $K_\alpha^\star$ is to use the *corner complex scaling* technique introduced in [10]. This technique has proven successful to compute embedded eigenvalues and complex resonances in [11]; in this work the authors employ a 2D finite element method (FEM) for a problem closely related to (4), namely the *plasmonic eigenvalue problem* (PEP).

Definition 3 (PEP)**.** Find $(u, \kappa) \in \dot{H}^1(\mathbb{R}^2) \times (-\infty, 0)$, $u \neq 0$, such that

$$\nabla \cdot [a(\boldsymbol{x}, \kappa) \nabla u(\boldsymbol{x})] = 0 \tag{5a}$$

$$u(\boldsymbol{x}) \underset{|\boldsymbol{x}| \to \infty}{=} O(|\boldsymbol{x}|^{-1}) \tag{5b}$$

where

$$\dot{H}^1(\mathbb{R}^2) := \left\{ u \in L^2_{\mathrm{loc}}(\mathbb{R}^2) \;\middle|\; \nabla u \in L^2(\mathbb{R}^2) \right\}, \; a(\boldsymbol{x}, \kappa) = \begin{cases} 1 & (\boldsymbol{x} \in \Omega) \\ \kappa & (\boldsymbol{x} \in \Omega^c). \end{cases}$$

The link between (4) and (5) will be stated precisely in Section 2.1; for now let us simply state that the two spectral parameters are linked by a Möbius transformation:

$$2\lambda = \frac{\kappa + 1}{\kappa - 1}, \; \kappa = \frac{2\lambda + 1}{2\lambda - 1} \quad (\Re(\kappa) < 0, \, |\lambda| < 1/2). \tag{6}$$

The main question we answer in this work is therefore: how can one carry over a complex scaling technique developed for (5) to (4)? We follow ideas from [12] and [13], where complex-scaled Green's functions are introduced to deal with scattering problems posed on domains with infinite boundaries: the surprising connection between these two works and (4) is that each corner in Γ can be viewed as a semi-infinite waveguide [14, § 4]. The numerical results presented in Section 5 demonstrate the advantage of discretizing $K_\alpha^\star$ over the FEM proposed in [11].

This article is organized as follows. The remainder of this introduction summarizes the theoretical and computational literature on (4,5). Section 2 summarizes some background results. Section 3 derives the complex-scaled PEP and introduces the complex-scaled NP operator $K_\alpha^\star$. Section 4 derives a closed-form expression of the complex-scaled Green's function, leading to the expression (35). Section 5 describes the employed Nyström method and gathers numerical validation and results[2]. Appendix A gathers standard results on BI operators associated with strongly elliptic equations. Appendix B contains the straightforward but tedious computations that are needed to derive the complex-scaled NP operator.

Remark 4 (Physical motivation). In (5), Ω models a metallic particle included in an infinite dielectric medium. The spectral parameter κ is a ratio of dielectric permittivities known as the *contrast*, while u is known as a *localized surface plasmon* [15, Chap. 5] [16, Chap. 9] [17]. The problem (5) can be interpreted as either Gauss' equation[3] or the quasi-static approximation of the transverse magnetic Maxwell equations[4].

[2] Code available online at https://doi.org/10.5281/zenodo.16309756.

[3] Then u is the electric potential, σ the dielectric permittivity ε, and $\kappa = \varepsilon_d/\varepsilon_m$.

[4] Then u is the z-component of the magnetic field, σ is the inverse of the dielectric permittivity, and $\kappa = \varepsilon_m/\varepsilon_d$.

1.1. Spectral theory of the NP operator

The spectral theory of the NP operator is widely developed [4, 18, 19]. Since Ω has a Lipschitz boundary, the NP operator is similar to a bounded self-adjoint operator [20, Prop. 3.3] and its spectrum satisfies [21, Thm. 2] [22, Thm. 2.5]

$$\sigma(K^\star) \subset [-1/2, 1/2),$$

where $\lambda = -1/2$ is a pathological eigenvalue not associated with a solution of the PEP [23, Thm. 4.2]. The structure of the spectrum depends crucially upon the regularity of the boundary. When $N_c = 0$, Ω has a C^2 boundary so that $\partial_\nu G$ is continuous on $\Gamma \times \Gamma$ and $K^\star$ is a compact operator, whose point and essential spectrum satisfy [24, 6]

$$\sigma_{\text{ess}}(K^\star) = \{0\},\ \sigma_p(K^\star) = \{\lambda_n\}_{n\geq 1} \cup \{-1/2\},\ \lim_{n\to\infty} \lambda_n = 0.$$

Equivalently, it has been proven that solutions (u_n, κ_n) of the PEP satisfy [25, Thm. 1]

$$\kappa_n < 0,\ \lim_{n\to\infty} \kappa_n = -1,$$

with each u_n localized around Γ [26, 27]. When $N_c \neq 0$, each corner contributes an interval to the essential spectrum: [5, Thm. 7] [28, Thm. 5.2] [29]

$$\sigma_{\text{ess}}(K^\star) = \bigcup_{k\in[\![1,N_c]\!]} \left[-\lambda_c(\phi_k), \lambda_c(\phi_k)\right],\ \lambda_c(\phi) \coloneqq \frac{|\phi - \pi|}{2\pi}. \tag{7}$$

The k-th interval of essential spectrum is linked to the existence of strongly-oscillating singularities that solve (5a) around the k-th corner [14], a fact we will elaborate upon in this work.

Li and Shipman have shown in [2] how one can construct curvilinear polygons Γ such that $K^\star$ exhibit *embedded eigenvalues*. Moreover, the existence of these embedded eigenvalues goes in pair with the existence of *complex resonances*, which can be generically defined as singularities of the continuation of the resolvent operator accross the essential spectrum [9]. The idea of the construction found by Li and Shipman is a perturbation mechanism that we will use in this work to design numerical validation cases.

1.2. Numerical computation of the NP spectrum

In the literature, both the boundary integral equation (BIE) (4) and the PEP (5) have been considered to compute isolated or embedded eigenvalues.

When $N_c = 0$, the continuity of the kernel of $K^\star$ implies that (4) can be accurately discretized using standard methods like Nyström [19, § 2.4.5] or Galerkin [30, § VI]. By contrast, conforming FEMs for (5) suffer from spectral pollution when using an unstructured mesh [31, § 6.2] [32, § 4.3]; this spectral pollution can be eliminated by using a mesh that is symmetric with respect to Γ [33]. When solving a direct problem, this limitation of conforming FEMs can be circumvented using a reformulation as an optimal control problem [34, 35].

When $N_c \neq 0$, the corner singularities associated with the essential spectrum induces numerical difficulties. For example, a Nyström discretization of (4) or a conforming FEM for (5) can only capture (real) eigenvalues located *outside* the essential spectrum: two remedies are available in the literature.

In [1], a method to compute embedded eigenvalues is introduced, which consists in computing the rate-of-resonance for all $\lambda \in (-1/2, 1/2)$ using a Nyström discretization of the regularized

operator $K^\star - (\lambda + i\varepsilon)\, I$ for $0 < \epsilon \ll 1$. The accuracy of the computed rate-of-resonance is ensured by using a multigrid preconditioning technique, known as the Recursively Compressed Inverse Preconditioning (RCIP) [36, 37], which avoids using an overly-refined graded mesh at corners. For an ellipse perturbed by a corner, this method is able to compute the first embedded eigenvalues and even detect the presence of complex resonances, although the imaginary part of the latter cannot be computed [1, Fig. 6].

In [11], a FEM able to compute both embedded eigenvalues and complex resonances is studied, which relies on the corner complex scaling technique introduced in [10]; the effectiveness of the method is demonstrated on the perturbed ellipse originally introduced in [1]. The computation relies on a linear generalized non-hermitian eigenvalue problem, which can be readily solved using standard packages. However, the main practical difficulty is meshing, since the mesh must not only satisfy the symmetry constraints discussed above to avoid spectral pollution, but it must also be disconnected since to ensure accuracy a neighborhood of the corner is discretized in a non-Cartesian coordinate system (see [11, Fig. 18]).

2. Notation and background

This section introduces notation and recalls a few facts that we will rely upon. Section 2.1 states the equivalence between the eigenvalue problems (4) and (5). In Section 2.2, this equivalence leads to a characterization of $\sigma_{\text{ess}}(K^\star)$ involving the corner singularities of (5a), which is the basis of the complex scaling technique used in this work. Finally, Section 2.3 recalls a characterization of complex resonances.

Notation. Let us first introduce some notation. We denote the jumps across Γ as

$$[\![f]\!]_\Gamma(\boldsymbol{x}) = f^+(\boldsymbol{x}) - f^-(\boldsymbol{x}), \quad [\![b\partial_\nu f]\!]_\Gamma(\boldsymbol{x}) = b^+\partial_\nu^+ f(\boldsymbol{x}) - b^-\partial_\nu^- f(\boldsymbol{x}) \quad (\boldsymbol{x} \in \Gamma), \tag{8}$$

where the superscript "+" (resp. "−") denotes the restriction to $\Omega^+ = \Omega^c$ (resp. $\Omega^- = \Omega$). For instance, the transmission conditions implied by (5a) can be written explicitly as

$$[\![u]\!]_\Gamma = 0 \text{ in } H^{1/2}(\Gamma), \quad [\![a(\cdot,\kappa)\partial_\nu u]\!]_\Gamma = 0 \text{ in } H^{-1/2}(\Gamma). \tag{9}$$

Using the free space Green's function of the Laplace operator, we define the *single layer potential* $\mathcal{S} : H^{-1/2}(\Gamma) \to H^1_{\text{loc}}(\mathbb{R}^2)$ and the *single layer operator* $S \in \mathcal{B}(H^{-1/2}(\Gamma), H^{1/2}(\Gamma))$:

$$\mathcal{S}\sigma(\boldsymbol{x}) \coloneqq \int_\Gamma G(\boldsymbol{x},\boldsymbol{y})\sigma(\boldsymbol{y})\,\mathrm{d}s(\boldsymbol{y}) \quad (\boldsymbol{x} \in \mathbb{R}^2), \quad S\sigma(\boldsymbol{x}) \coloneqq \int_\Gamma G(\boldsymbol{x},\boldsymbol{y})\sigma(\boldsymbol{y})\,\mathrm{d}s(\boldsymbol{y}) \quad (\boldsymbol{x} \in \Gamma),$$

the former satisfying *jump relations*

$$[\![\mathcal{S}\sigma]\!]_\Gamma = 0, \quad \partial_\nu^\pm \mathcal{S}\sigma = K^\star\sigma \mp \frac{1}{2}\sigma. \tag{10}$$

Layers potentials and BI operators can more generally be defined for any strongly elliptic equations having smooth coefficients: we have gathered in Appendix A the few standard results that we will rely on in this work.

2.1. Equivalence between the NP and plasmonic eigenvalue problems

Using the single layer potential $\mathcal{S}$, we can state the link between (4) and (5) as follows.

Proposition 5. *If $(\kappa, \lambda) \in (-\infty, 0) \times (-1/2, 1/2)$ are two scalars satisfying (6), then*

$$\exists\, \sigma \in H^{-1/2}(\Gamma)\backslash\{0\} \text{ that solves (4)} \Rightarrow u = \mathcal{S}\sigma \in \dot{H}^1(\mathbb{R}^2)\backslash\{0\} \text{ solves (5)},$$
$$\exists\, u \in \dot{H}^1(\mathbb{R}^2)\backslash\{0\} \text{ that solves (5)} \Rightarrow \sigma = -[\![\partial_\nu u]\!]_\Gamma \in H^{-1/2}(\Gamma)\backslash\{0\} \text{ solves (4)}.$$

Proof. This result is standard [38, 39, 30, 40] and effectively boils down to formulating an ansatz and exploiting the jump relations (10). For the sake of completeness, the proof is given in Appendix A, see Proposition 31: this proposition covers a slightly more general case, in anticipation of our study of corner complex scaling. □

2.2. Characterization of the essential spectrum

To clarify the exposition, we now assume that $N_c = 1$, i.e. that there is only one corner of angle ϕ at $\boldsymbol{x_c}$ (see Figure 1b). The equivalence stated in Proposition 5 implies that we can understand the corner behavior of a density solving (4) by studying solutions of (5a). The next result gives the corner behavior of eigenfunctions, associated with either isolated or embedded eigenvalues.

Proposition 6. *Let $\lambda \in (-1/2, 1/2)\backslash\{0\}$. Let $\kappa \in (-\infty, 0)\backslash\{-1\}$ be given by (6). If $u \in \dot{H}(\mathbb{R}^2)$ solves (5a) then, for any $\beta > 0$, u satisfies the corner expansion*

$$u(r,\theta) \underset{r\to 0}{=} c_0 + \sum_{\rho\in\{\mathfrak{e},\mathfrak{o}\}} \sum_{\substack{\eta\in H(\lambda,\rho)\\ -\beta<\Im(\eta)<0}} c_\eta^\rho r^{i\eta}\Phi^\rho(\theta,\eta) + O(r^\beta), \tag{11}$$

where the even ("$\mathfrak{e}$") and odd ("$\mathfrak{o}$") orthoradial functions are

$$\Phi^\rho(\theta,\eta) := \begin{cases} \dfrac{\cosh(\eta\theta)}{\cosh(\eta\phi/2)}\mathbb{1}_\Omega(\theta) + \dfrac{\cosh(\eta(\pi-|\theta|))}{\cosh(\eta(\pi-\phi/2))}\mathbb{1}_{\Omega^c}(\theta) & \text{if } \rho = \mathfrak{e} \\ \dfrac{\sinh(\eta\theta)}{\sinh(\eta\phi/2)}\mathbb{1}_\Omega(\theta) + \dfrac{\sinh(\eta(\pi-|\theta|))}{\sinh(\eta(\pi-\phi/2))}\mathbb{1}_{\Omega^c}(\theta) & \text{if } \rho = \mathfrak{o}, \end{cases}$$

with $\mathbb{1}_X$ the characteristic function of X, and the set of radial exponent H is defined as

$$H(\lambda,\rho) := \{\eta \in \mathbb{C}^* \mid g^\rho(\eta,\lambda) = 0\},$$

with $g^\mathfrak{e}$ and $g^\mathfrak{o}$ the meromorphic functions

$$g^\mathfrak{e}(\eta,\lambda) := 2\lambda + \frac{\sinh[\eta(\pi-\phi)]}{\sinh[\eta\pi]},\quad g^\mathfrak{o}(\eta,\lambda) := 2\lambda - \frac{\sinh[\eta(\pi-\phi)]}{\sinh[\eta\pi]}. \tag{12}$$

Proof (sketch). This result can be intuitively understood by injecting the ansatz $u(r,\theta) = r^{i\eta}w(\theta)$ in (5a) to obtain an ordinary differential equation (ODE) in θ that admits even (resp. odd) non-null solutions if and only if $g^\mathfrak{e}(\eta,\lambda) = 0$ (resp. $g^\mathfrak{o}(\eta,\lambda) = 0$), see [10, Prop. 3.1]. The proof can be carried out using tools that are standard in the study of elliptic equations on domains with

corners [41, 42, 43] and consists in [44, 45]: (i) localizing (5a) around the corner by working on $v = \chi u$ with $\chi \in C_c^\infty(\mathbb{R}^2)$ equal to 1 around $\boldsymbol{x_c}$, (ii) applying the Mellin transform

$$\hat{v}(\eta,\theta) = \int_0^\infty v(r,\theta) r^{-(i\eta+1)}\,\mathrm{d}r,\ \ v(r,\theta) = \frac{1}{2\pi}\int_{-\infty+i\gamma}^{+\infty+i\gamma} \hat{v}(\eta,\theta) r^{i\eta}\,\mathrm{d}\eta \quad (\gamma > 0),$$

to obtain an ODE in θ parametrized by η, (iii) solving the ODE, and (iv) inverting the Mellin transform by closing the contour in $\{-\beta \le \Im(\eta) \le 0\}$ using the residue theorem. □

In the expansion (11), all the factors $r^{i\eta}$ vanish at the corner since $\Im(\eta) < 0$. The limiting case $\Im(\eta) = 0$ leads to *strongly-oscillating corner singularities*[5]

$$\mathfrak{s}^{\mathfrak{e}\,(\mathfrak{o})}(r,\theta,\eta) \coloneqq r^{i\eta}\Phi^{\mathfrak{e}\,(\mathfrak{o})}(\theta,\eta) \quad (\eta \in \mathbb{R}^*), \tag{13}$$

which belong to $L^2_{\mathrm{loc}}(\mathbb{R}^2)$ but not $H^1_{\mathrm{loc}}(\mathbb{R}^2)$; a plot of the even singularity $\mathfrak{s}^{\mathfrak{e}}$ is given in Figure 2a. A distinctive feature of these singularities is that they radiate energy to or from the corner, i.e. they satisfy $J(\mathfrak{s}) \neq 0$, where J is the *corner energy flux* [10, (26)]:

$$J(u) \coloneqq \lim_{\varepsilon\to 0} \Im\left[\int_{\partial B(\boldsymbol{x_c},\varepsilon)} a(\boldsymbol{x},\kappa) u(\boldsymbol{x}) \overline{\partial_r u(\boldsymbol{x})}\,\mathrm{d}s(\boldsymbol{x})\right],$$

which is positive (resp. negative) if u radiates from (resp. to) the corner. The equivalence stated in Proposition 5 suggests that the essential spectrum of $K^\star$ can be understood as the set of λ such that the expansion (11) contains a strongly-oscillating singularity (either odd or even), which writes

$$\sigma_{\mathrm{ess}}(K^\star) = \bigcup_{\rho\in\{\mathfrak{e},\mathfrak{o}\}} \sigma^\rho_{\mathrm{ess}}(K^\star),\ \ \sigma^\rho_{\mathrm{ess}}(K^\star) = \overline{\{\lambda\in\mathbb{C} \mid \exists \eta\in\mathbb{R}^* :\ g^\rho(\eta,\lambda) = 0\}},$$

which does match the known formula (7) for $N_c = 1$ since from (12):

$$\sigma^{\mathfrak{o}}_{\mathrm{ess}}(K^\star) = -\sigma^{\mathfrak{e}}_{\mathrm{ess}}(K^\star),\ \ \sigma^{\mathfrak{e}}_{\mathrm{ess}}(K^\star) = \begin{cases} [-\lambda_c(\phi), 0] & \text{if } \phi\in(0,\pi) \\ [0,\lambda_c(\phi)] & \text{if } \phi\in(\pi,2\pi). \end{cases}$$

We are now in a position to state the following characterization of $\sigma_{\mathrm{ess}}(K^\star)$, which will be our starting point to study complex scaling.

Proposition 7. *Let $\rho \in \{\mathfrak{e},\mathfrak{o}\}$ and $\lambda \in \sigma^\rho_{\mathrm{ess}}(K^\star)\backslash\{0,\pm\lambda_c(\phi)\}$. Let κ be given by (6). Up to a multiplicative constant, there is a unique non-null function $u \in \dot{H}^1(\mathbb{R}^2\backslash\{\boldsymbol{x_c}\})$ that solves (5) and satisfies $J(u) < 0$. Moreover, this function satisfies the corner expansion*

$$u(r,\theta) \underset{r\to 0}{=} r^{i\eta_s}\Phi^\rho(\theta,\eta_s) + c_0 + O(|r^{i\eta_t}|), \tag{14}$$

where the singular exponent η_s is the unique non-null real solution of $g^\rho(\eta_s,\lambda) = 0$ that satisfy $\lambda\eta_s < 0$ and the truncation exponent η_t is the solution of $g^{\mathfrak{e}}(\eta_t,\lambda)g^{\mathfrak{o}}(\eta_t,\lambda) = 0$ with the largest negative imaginary part.

Remark 8. The corresponding expansion of the boundary density is deduced using Proposition 5.

[5] These should not be confused with elliptic singularities [42], which behave like r^η for $\eta > 0$ and belong to H^1_{loc}.

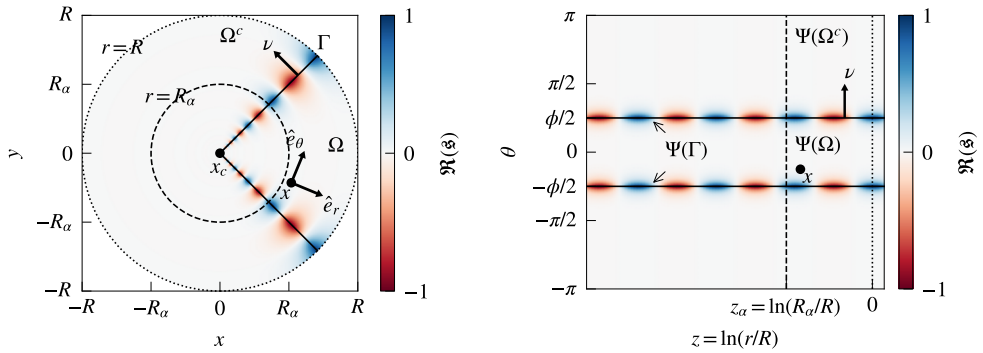

(a) Cartesian coordinates.

(b) Euler coordinates.

Figure 2: Even strongly-oscillating singularity (13) in a neighborhood of a straight corner at $\boldsymbol{x_c}$. (Left) Cartesian coordinates. (Right) Euler coordinates (16), which map $r^{i\eta}$ to $e^{i\eta z}$.

Remark 9. The strongly-oscillating singularity in (14) makes computing the essential spectrum challenging.

Proof (sketch). We refer to [14] for a treatment of the condition $J(u) < 0$, called a corner radiation condition, in radially-weighted Sobolev spaces; we provide here a formal summary of the computations leading to the claim. Let $\rho \in \{\mathfrak{e}, \mathfrak{o}\}$ and $\lambda \in \sigma^{\rho}_{\mathrm{ess}}(K^\star)\backslash\{0, \pm\lambda_c(\phi)\}$. The key result is that the map $g^\rho(\cdot, \lambda)$ admits exactly two non-null real zeros of opposite sign: $\eta_c > 0$ and $-\eta_c < 0$. The steps highlighted in the proof sketch of Proposition 6 can be carried out identically; the only difference is that when closing the contour in the lower half-plane $\{\Im(\eta) \le 0\}$ we pick up the two real poles $\pm\eta_c$, leading to the corner expansion, for any $\beta > 0$:

$$u(r,\theta) \underset{r\to 0}{=} c_+ \mathfrak{s}^\rho(r,\theta,\eta_c) + c_- \mathfrak{s}^\rho(r,\theta,-\eta_c) + c_0 + \sum_{\mu\in\{\mathfrak{e},\mathfrak{o}\}} \sum_{\substack{\eta\in H(\lambda,\mu)\\ -\beta<\Im(\eta)<0}} c^\mu_\eta r^{i\eta}\Phi^\mu(\theta,\eta) + O(r^\beta).$$

This expansion contains two singular coefficients $c_\pm$ associated with the two (complex-conjugated) strongly-oscillating singularities. Since we assume $J(u) \neq 0$, we must have $c_+ \neq 0$ or $c_- \neq 0$, since otherwise we would have $u \in H^1_{\mathrm{loc}}(\mathbb{R}^2)$ and therefore $J(u) = 0$. In fact, the requirement that $J(u) < 0$ implies that exactly one singular coefficient is non-null [10, Tab. 1]: if $\lambda > 0$ (resp. $\lambda < 0$) then $c_- \neq 0$ (resp. $c_+ \neq 0$) and we define the singular exponent as $\eta_s = -\eta_c$ (resp. $\eta_s = +\eta_c$). The truncation exponent η_t is the dominant exponent in the remainder. □

2.3. Characterization of complex resonances

Let us conclude this background section by discussing complex resonances (we refer to [9] for the general theory). Since the spectrum of $K^\star$ is real, the *resolvent operator*

$$\mathcal{R}: \ \{\lambda \in \mathbb{C} \,|\, \Im(\lambda) > 0\} \mapsto \mathcal{B}(H^{-1/2}(\Gamma), H^{-1/2}(\Gamma)), \ \lambda \mapsto (K^\star - \lambda I)^{-1},$$

defines an analytic family of bounded linear operators. The essential spectrum is a branch cut for $\mathcal{R}$, with branch points at 0 and $\pm\lambda_c(\phi)$. By crossing the essential spectrum once, either through $(-\lambda_c(\phi), 0)$ or $(0, \lambda_c(\phi))$, one obtains two distinct meromorphic continuations of $\mathcal{R}$, denoted $\mathcal{R}^{\mathfrak{e}}$ and $\mathcal{R}^{\mathfrak{o}}$, whose singularities are complex resonances; this is captured in the following abstract definition.

Definition 10. A scalar $\lambda \in \mathbb{C}\backslash\mathbb{R}$ is a *complex resonance* if it is an isolated singularity of either $\mathcal{R}^{\mathfrak{e}}$ or $\mathcal{R}^{\mathfrak{o}}$.

More importantly for numerical computations, by continuation on λ in Proposition 6, we deduce that complex resonances are associated with solutions of (5) in $\mathbb{R}^2\backslash\{\boldsymbol{x_c}\}$ that behave like (14) for some $\eta_s \in H(\lambda, \rho)$ such that $\Im(\eta_s) > 0$. In particular, these solutions are singular at the corner and thus are not eigenfunctions. The corner complex scaling technique will enable us to compute complex resonances as eigenvalues of a modified problem.

3. Corner complex scaling for the Neumann-Poincaré operator

In this section we obtain the complex-scaled NP operator (31) by applying the corner complex scaling from [10] to the NP operator. This section is organized as follows. Section 3.1 introduces the scaling technique in a non-Cartesian coordinate system, where an intuitive waveguide analogy can be relied upon. Section 3.2 then derives the scaling in Cartesian coordinates, which is used in Section 3.3 to introduce the complex-scaled NP operator. Finally, Section 3.4 illustrates that the effect of complex scaling is to move the essential spectrum away from the real axis, uncovering both embedded eigenvalues and complex resonances in the process. Throughout this section, we assume that $N_c = 1$ to simplify the exposition.

3.1. A waveguide analogy in Euler coordinates

Let $\rho \in \{\mathfrak{e}, \mathfrak{o}\}$ and $\lambda \in \sigma^{\rho}_{\text{ess}}(K^\star)$ such that $\lambda \neq 0$ and $|\lambda| \neq \lambda_c(\phi)$. From Proposition 7, this value of λ is associated with a solution of (5) that is strongly-oscillating at the corner:

$$\nabla \cdot [a(\boldsymbol{x}, \kappa)\nabla u] = 0 \quad (x \in B(\boldsymbol{x_c}, R)\backslash\{\boldsymbol{x_c}\}), \tag{15a}$$

$$u(r, \theta) \underset{r\to 0}{=} r^{i\eta_s}\Phi^{\rho}(\theta, \eta_s) + c_0 + O(|r^{i\eta_t}|), \tag{15b}$$

where $R > 0$ is a radius chosen small enough (ref. Assumption 1), κ is given by (6), the singularity exponent η_s is real, and $\Im(\eta_t) < 0$. From Proposition 5, the corresponding strongly-oscillating boundary density satisfies

$$K^\star\sigma = \lambda\sigma, \ \sigma(r, \theta) \underset{r\to 0}{=} -r^{i\eta_s}[\![\partial_\theta\Phi^{\rho}]\!]_\Gamma(\theta, \eta_s) + O(|r^{i\eta_t}|).$$

The corner complex scaling technique enables to tame the singular term $r^{i\eta_s}$, which is the source of numerical difficulties. We follow here the original exposition [10] by introducing the *Euler coordinate system* (z, θ):

$$\Psi : \mathbb{R}^2\backslash\{\boldsymbol{x_c}\} \to \mathbb{R} \times (-\pi, \pi), \ (x, y) \mapsto (z, \theta) := (\ln(r/R), \theta). \tag{16}$$

This mapping, illustrated in Figure 2b, sends $\boldsymbol{x_c}$ to $-\infty$, the boundary $\Gamma \cap B(\boldsymbol{x_c}, R)$ to the straight line $\{z < 0, \theta = \pm\phi/2\}$, and transforms (15) into

$$\nabla_{(z,\theta)} \cdot [a(\theta, \kappa)\nabla_{(z,\theta)}\tilde{u}](z, \theta) = 0 \quad ((z, \theta) \in S := (-\infty, 0) \times (-\pi, \pi)), \tag{17a}$$

$$\tilde{u}(z, \theta) \underset{z\to-\infty}{=} e^{i\eta_s z}\Phi^{\rho}(\theta, \eta_s) + c_0 + O(|e^{i\eta_t z}|), \tag{17b}$$

$$\tilde{u}(z, -\pi) = \tilde{u}(z, \pi), \ \partial_\theta\tilde{u}(z, -\pi) = \partial_\theta\tilde{u}(z, \pi), \tag{17c}$$

where $\tilde{u} \coloneqq u \circ \Psi^{-1}$ and

$$\nabla_{(z,\theta)} f \coloneqq \frac{1}{Re^z} \begin{bmatrix} \partial_z f \\ \partial_\theta f \end{bmatrix}, \quad \nabla_{(z,\theta)} \cdot \begin{bmatrix} f_1 \\ f_2 \end{bmatrix} \coloneqq \frac{1}{R^2 e^{2z}} \left[\partial_z (Re^z f_1) + \partial_\theta (Re^z f_2) \right].$$

The benefit of this process is that (17b) is similar to a waveguide radiation condition, which can be dealt with using a linear complex scaling [46, 47]. The idea of complex scaling is to stretch the z coordinate as $z \mapsto z/\alpha$ where $\alpha \in \mathbb{C}^*$ is a *scaling parameter*. To make this precise we introduce the continuous complex-valued path

$$\tilde{\Gamma}_\alpha : \mathbb{R} \times (-\pi, \pi) \to \mathbb{C} \times (-\pi, \pi), (z, \theta) \mapsto (\tilde{\gamma}(z), \theta), \tag{18}$$

where $\tilde{\gamma} : \mathbb{R} \to \mathbb{C}$ defines the linear coordinate scaling:

$$\tilde{\gamma}(z) \coloneqq \begin{cases} z & (z > z_\alpha) \\ (z - z_\alpha)/\alpha + z_\alpha & (z < z_\alpha), \end{cases} \quad \tilde{\gamma}'(z) = \begin{cases} 1 & (z > z_\alpha) \\ 1/\alpha & (z < z_\alpha), \end{cases}$$

with $z_\alpha = \ln(R_\alpha/R)$ and $R_\alpha \in (0, R)$ the radius delimiting the entrance of the *scaling region*. The effect of this scaling on strongly-oscillating singularities (13) is illustrated in Figure 3. Using the scaling path we define the *scaled solution* $\tilde{u}_\alpha$ as

$$\tilde{u}_\alpha(z, \theta) \coloneqq \tilde{u} \circ \tilde{\Gamma}_\alpha(z, \theta) = \tilde{u}(\tilde{\gamma}(z), \theta) \quad ((z, \theta) \in \mathbb{R} \times (-\pi, \pi)),$$

where on the right-hand side $\tilde{u}(\cdot, \theta)$ denotes the analytic continuation of $\tilde{u}(\cdot, \theta)$, which is an abuse of notation. Using the chain rule we deduce that $\tilde{u}_\alpha$ solves

$$\nabla_{(z,\theta)} \cdot [a(\theta, \kappa) \tilde{A}_\alpha(z) \nabla_{(z,\theta)} \tilde{u}_\alpha](z, \theta) = 0 \quad ((z, \theta) \in S), \tag{19a}$$

$$\tilde{u}_\alpha(z, \theta) \underset{z \to -\infty}{=} e^{i\eta_s z/\alpha} \Phi^\rho(\theta, \eta_s) + c_0 + O(|e^{i\eta_t z/\alpha}|), \tag{19b}$$

$$\tilde{u}_\alpha(z, -\pi) = \tilde{u}_\alpha(z, \pi), \ \partial_\theta \tilde{u}_\alpha(z, -\pi) = \partial_\theta \tilde{u}_\alpha(z, \pi), \tag{19c}$$

where the *scaling matrix* $\tilde{A}_\alpha$ is

$$\tilde{A}_\alpha(z) = \begin{bmatrix} 1/\tilde{\gamma}'(z) & 0 \\ 0 & \tilde{\gamma}'(z) \end{bmatrix} = \begin{cases} I & (z > z_\alpha) \\ \mathrm{diag}(\alpha, 1/\alpha) & (z < z_\alpha). \end{cases}$$

The computational interest of (19) over (15) and (17) lies in the ability to choose α such that $\tilde{u}_\alpha$ decays exponentially as $z \to -\infty$. Unfortunately, the discretization of this scaled problem is somewhat laborious since it requires dealing with the coupling between the Euler domain S (one per corner in case of multiple corners) and the Cartesian domain $\mathbb{R}^2 \backslash B(\boldsymbol{x_c}, R)$, see [10] for a FEM treatment with three corners. To avoid dealing with this coupling in our BIE, we now derive a purely Cartesian formulation of (19).

3.2. Corner complex scaling in Cartesian coordinates

To work in the whole of $\mathbb{R}^2$, we introduce the piecewise-constant scaling function

$$\hat{\alpha}(\boldsymbol{x}) \coloneqq \frac{1}{\tilde{\gamma}'(z(\boldsymbol{x}))} = \begin{cases} \alpha & \boldsymbol{x} \in B_\alpha \coloneqq B(\boldsymbol{x_c}, R_\alpha) \\ 1 & \boldsymbol{x} \notin B_\alpha. \end{cases}$$

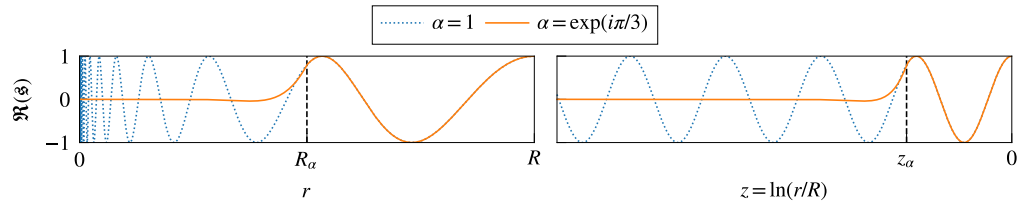

Figure 3: Strongly-oscillating singularity (13) with complex scaling (18). (Left) As a function of r. (Right) As a function of z given by (16).

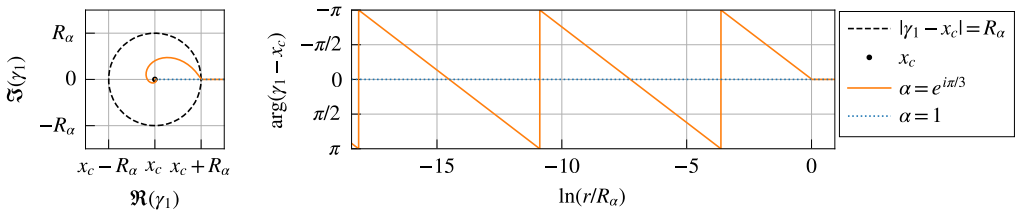

Figure 4: Complex scaling path Γ_α: plot of $r \mapsto \gamma_1(x_c + r, y_c)$ for $r \in (0, 1.5R_\alpha)$.

Mimicking Section 3.1, we define the complex-scaling path as $\Gamma_\alpha := \Psi^{-1} \circ \tilde{\Gamma}_\alpha \circ \Psi$, i.e.

$$\Gamma_\alpha : \mathbb{R}^2 \to \mathbb{C}^2, \ \boldsymbol{x} \mapsto (\gamma_1(\boldsymbol{x}), \gamma_2(\boldsymbol{x})) = \boldsymbol{x_c} + \mu_\alpha(\boldsymbol{x})[\boldsymbol{x} - \boldsymbol{x_c}], \tag{20}$$

where the radial scaling function $\mu_\alpha \in C^0(\mathbb{R}^2 \backslash \{\boldsymbol{x_c}\}; \mathbb{C})$ is

$$\mu_\alpha(\boldsymbol{x}) := \left(\frac{|\boldsymbol{x} - \boldsymbol{x_c}|}{R_\alpha} \right)^{\frac{1}{\hat{\alpha}(\boldsymbol{x})} - 1}. \tag{21}$$

Comparison between (18) and (20) highlights that, whereas $\tilde{\Gamma}_\alpha$ only scales the z coordinate linearly, Γ_α scales both x and y coordinates non-linearly; Figure 4 shows that γ_1 spirals around $(x_c, 0)$ with a logarithmically-varying argument. The regularity of Γ_α is as follows.

Lemma 11. *Let $\Re(\alpha) > 0$. The scaling path has the following regularity: $\Gamma_\alpha \in C^0(\mathbb{R}^2) \cap C^\infty(\mathbb{R}^2 \backslash [\{\boldsymbol{x_c}\} \cup \partial B_\alpha])$ with Jacobian matrix*

$$J_\alpha(\boldsymbol{x}) := \begin{pmatrix} \partial_x \gamma_1(\boldsymbol{x}) & \partial_y \gamma_1(\boldsymbol{x}) \\ \partial_x \gamma_2(\boldsymbol{x}) & \partial_y \gamma_2(\boldsymbol{x}) \end{pmatrix} = \mu_\alpha(\boldsymbol{x}) \left[I + \left(\frac{1}{\hat{\alpha}(\boldsymbol{x})} - 1 \right) P_c(\boldsymbol{x}) \right], \tag{22}$$

where $P_c(\boldsymbol{x})$ is the orthogonal projection on span $(\boldsymbol{x} - \boldsymbol{x_c})$*:*

$$P_c(\boldsymbol{x}) := \frac{1}{|\boldsymbol{x} - \boldsymbol{x_c}|^2} \begin{bmatrix} (x - x_c)^2 & (x - x_c)(y - y_c) \\ (x - x_c)(y - y_c) & (y - y_c)^2 \end{bmatrix} \quad (\boldsymbol{x} \neq \boldsymbol{x_c}). \tag{23}$$

Remark 12. If $\boldsymbol{x} \notin \overline{B_\alpha}$, then $\Gamma_\alpha(\boldsymbol{x}) = \boldsymbol{x}$ and $J_\alpha = I$.

Proof. Let $\Re(\alpha) > 0$. The continuity of Γ_α at any $\boldsymbol{x} \neq \boldsymbol{x_c}$ is straightforward; continuity at $\boldsymbol{x_c}$ is a consequence of $|\Gamma_\alpha(\boldsymbol{x}) - \boldsymbol{x_c}| \underset{\boldsymbol{x} \to \boldsymbol{x_c}}{=} O(|\boldsymbol{x} - \boldsymbol{x_c}|^{\Re(1/\alpha)})$. The expression of J_α follows from the chain rule using

$$\nabla_{\boldsymbol{x}} |\boldsymbol{x} - \boldsymbol{x_c}| = \frac{\boldsymbol{x} - \boldsymbol{x_c}}{|\boldsymbol{x} - \boldsymbol{x_c}|}, \ \nabla_{\boldsymbol{x}} \mu_\alpha(\boldsymbol{x}) = \left(\frac{1}{\hat{\alpha}(\boldsymbol{x})} - 1 \right) \mu_\alpha(\boldsymbol{x}) \frac{\boldsymbol{x} - \boldsymbol{x_c}}{|\boldsymbol{x} - \boldsymbol{x_c}|^2}.$$

□

Let $R_\alpha > 0$ be a radius such that u is real-analytic in B_α. The scaled solution is

$$u_\alpha \coloneqq u \circ \Gamma_\alpha,$$

where on the right-hand side u denotes the analytic continuation. Since $u_\alpha = \tilde{u}_\alpha \circ \Psi$, we can obtain the problem satisfied by u_α by a change of coordinates in (19), leading to the following.

Definition 13 (Complex-Scaled PEP)**.** Find $(u_\alpha, \kappa) \in \dot{H}^1(\mathbb{R}^2) \times \mathbb{C}$, $u_\alpha \neq 0$, such that

$$\nabla \cdot [a(\boldsymbol{x}, \kappa) A_\alpha(\boldsymbol{x}) \nabla u_\alpha(\boldsymbol{x})] = 0 \quad (\boldsymbol{x} \in \mathbb{R}^2) \tag{24a}$$

$$u_\alpha(\boldsymbol{x}) \underset{|\boldsymbol{x}|\to\infty}{=} O(|\boldsymbol{x}|^{-1}), \tag{24b}$$

where the scaling matrix is

$$A_\alpha(\boldsymbol{x}) = \frac{1}{\hat{\alpha}(\boldsymbol{x})} I + \left(\hat{\alpha}(\boldsymbol{x}) - \frac{1}{\hat{\alpha}(\boldsymbol{x})}\right) P_c(\boldsymbol{x}) \quad (\boldsymbol{x} \in \mathbb{R}^2 \backslash [\{\boldsymbol{x_c}\} \cup \partial B_\alpha]). \tag{25}$$

Proposition 14. *For any $\alpha \in \mathbb{C}^*$ and $\boldsymbol{x} \in \mathbb{R}^2 \backslash \{\{\boldsymbol{x_c}\} \cup \partial B_\alpha\}$,*

1. $A_\alpha \in L^\infty(\mathbb{R}^2) \cap C^\infty(\mathbb{R}^2 \backslash [\{\boldsymbol{x_c}\} \cup \partial B_\alpha])$.
2. $A_\alpha(\boldsymbol{x})^T = A_\alpha(\boldsymbol{x})$.
3. $A_\alpha(\boldsymbol{x})\hat{\boldsymbol{e}}_{\boldsymbol{r}}(\boldsymbol{x}) = \hat{\alpha}(\boldsymbol{x})\, \hat{\boldsymbol{e}}_{\boldsymbol{r}}(\boldsymbol{x})$ *and* $A_\alpha(\boldsymbol{x})\hat{\boldsymbol{e}}_{\boldsymbol{\theta}}(\boldsymbol{x}) = \frac{1}{\hat{\alpha}(\boldsymbol{x})}\hat{\boldsymbol{e}}_{\boldsymbol{\theta}}(\boldsymbol{x})$.

Proof. The first two claims follow directly from the definition of A_α. To show the third one, let $\boldsymbol{x} \in \mathbb{R}^2$ such that $\boldsymbol{x} \neq \boldsymbol{x_c}$ and $\boldsymbol{x} \notin \partial B_\alpha$. Let $(z, \theta) = \Psi(\boldsymbol{x}) \in S$ be the corresponding Euler coordinates. A computation shows that $A_\alpha(\boldsymbol{x})U(\theta) = U(\theta)\tilde{A}_\alpha(z)$, where

$$U(\theta) = \begin{pmatrix} \cos\theta & -\sin\theta \\ \sin\theta & \cos\theta \end{pmatrix} = (\hat{\boldsymbol{e}}_{\boldsymbol{r}}, \hat{\boldsymbol{e}}_{\boldsymbol{\theta}})\,. \tag{26}$$

□

Note that the matrix A_α is essentially bounded in $\mathbb{R}^2$ although it cannot be continuously extended to $\boldsymbol{x} = \boldsymbol{x_c}$. Due to the piecewise-constant definition of $\hat{\alpha}$, A_α has a jump discontinuity at the entrance of the scaling region ∂B_α: the transmission conditions implied by (24a) are (9) as well as

$$[\![u_\alpha]\!]_{\partial B_\alpha} = 0 \text{ in } H^{1/2}(\partial B_\alpha),\ [\![\hat{\alpha}\partial_r u_\alpha]\!]_{\partial B_\alpha} = 0 \text{ in } H^{-1/2}(\partial B_\alpha). \tag{27}$$

One could also choose a smooth coefficient $\hat{\alpha}$ to avoid this additional transmission condition on ∂B_α; our choice of $\hat{\alpha}$ is merely motivated by the simplicity of implementation. The next proposition, to be compared with Proposition 6, shows that the corner complex scaling rotates the radial exponents.

Proposition 15. *Let $\Re(\alpha) > 0$, $\lambda \in (-1/2, 1/2)\backslash\{0\}$ and κ given by (6). If $u \in \dot{H}(\mathbb{R}^2)$ solves (24a) then, for any $\beta > 0$, u satisfies the corner expansion*

$$u(r, \theta) \underset{r\to 0}{=} c_0 + \sum_{\rho\in\{\mathfrak{e},\mathfrak{o}\}} \sum_{\substack{\alpha\eta\in H(\lambda,\rho) \\ -\beta<\Im(\eta)<0}} c_\eta^\rho r^{i\eta} \Phi^\rho(\theta, \alpha\eta) + O(r^\beta). \tag{28}$$

Proof (sketch). The proof is identical to that sketched for Proposition 6: the only difference is that at every step, "η" is substituted with "$\alpha\eta$". □

3.3. Complex-scaled boundary integral operators

For any $\alpha \in \mathbb{C}^*$, we define the complex-scaled Laplacian:

$$\mathcal{P}_\alpha u(\boldsymbol{x}) = -\nabla \cdot [A_\alpha \nabla u](\boldsymbol{x}) \quad (\boldsymbol{x} \in \mathbb{R}^2),$$

where A_α is the scaling matrix (25), whose regularity is given in Proposition 14; when $\alpha = 1$, $\mathcal{P}_\alpha = -\Delta$. The key property is that $\mathcal{P}_\alpha$ is uniformly strongly elliptic on $\mathbb{R}^2$.

Proposition 16 (Strong ellipticity)**.** *If $\Re(\alpha) > 0$, then there are constants $c_0, c_1 > 0$ such that for almost every $x \in \mathbb{R}^2$ and all $\xi \in \mathbb{R}^2$,*

$$c_0|\xi|^2 \le \Re[A_\alpha(\boldsymbol{x})\xi \cdot \xi] \le c_1|\xi|^2.$$

Proof. Let $\boldsymbol{x} \in \mathbb{R}^2$ such that $\boldsymbol{x} \neq \boldsymbol{x_c}$ and $\boldsymbol{x} \notin \partial B_\alpha$. If $\boldsymbol{x} \notin B_\alpha$, then $A_\alpha(x)\xi \cdot \xi = |\xi|^2$, so that we now assume that $\boldsymbol{x} \in B_\alpha$. Let $(z, \theta) = \Psi(\boldsymbol{x}) \in S$ and $U(\theta)$ be the orthogonal matrix (26). For any $\xi \in \mathbb{R}^2$ we have with $w = U(\theta)^T \xi$:

$$\Re[A_\alpha(\boldsymbol{x})\xi \cdot \xi] = \Re[\tilde{A}_\alpha(z)w \cdot w] = \Re(\alpha)w_1^2 + \Re(1/\alpha)w_2^2,$$

so that $\min[\Re(\alpha), \Re(1/\alpha)]|\xi|^2 \le \Re[A_\alpha(\boldsymbol{x})\xi \cdot \xi] \le \max[\Re(\alpha), \Re(1/\alpha)]|\xi|^2$. □

In view of this result we now assume that $\Re(\alpha) > 0$. Let G_α denote the free space Green's function of $\mathcal{P}_\alpha$, which satisfies: for any $\boldsymbol{y} \in \mathbb{R}^2$, $G_\alpha(\cdot, \boldsymbol{y}) \in L^1_{\mathrm{loc}}(\mathbb{R}^2)$ and

$$-\nabla_x \cdot [A_\alpha(\boldsymbol{x})\nabla_x G_\alpha(\boldsymbol{x}, \boldsymbol{y})] = \delta(\boldsymbol{x} - \boldsymbol{y}) \quad (\boldsymbol{x} \in \mathbb{R}^2) \tag{29}$$

in the sense of distributions. Since $\hat{\alpha}$ has a jump discontinuity at the entrance of the scaling region ∂B_α, $G_\alpha(\cdot, \boldsymbol{y})$ satisfies the transmission conditions (27); as already mentioned, these transmission conditions can be avoided by choosing a smooth scaling coefficient $\hat{\alpha}$.

The strong ellipticity of $\mathcal{P}_\alpha$ enables to define the associated layer potentials and BI operators, see the already mentioned Appendix A for references. We denote $\partial_{\alpha\nu}$ the conormal derivative associated with $\mathcal{P}_\alpha$, defined strongly for any $\varphi \in C^\infty(\mathbb{R}^2)$ as

$$\partial_{\alpha\nu}\varphi(\boldsymbol{x}) := [A_\alpha(\boldsymbol{x})\nabla\varphi(\boldsymbol{x})] \cdot \boldsymbol{\nu}(\boldsymbol{x}) \quad (\boldsymbol{x} \in \Gamma,\ \boldsymbol{x} \neq \boldsymbol{x_c},\ \boldsymbol{x} \notin \partial B_\alpha),$$

Using the first Green identity, this conormal derivative defines two one-sided trace operators $\partial^\pm_{\alpha\nu} : H^1_\alpha(\Omega^\pm) \to H^{-1/2}(\Gamma)$ where

$$H^1_\alpha(\Omega^\pm) = \{u \in H^1(\Omega^\pm) \,|\, \mathcal{P}_\alpha u \in L^2(\Omega^\pm)\}$$

is a subset of $H^1(\Omega^\pm)$ that includes the transmission conditions (27). The complex-scaled single layer potential and operator are

$$\mathcal{S}_\alpha\sigma(\boldsymbol{x}) := \int_\Gamma G_\alpha(\boldsymbol{x}, \boldsymbol{y})\sigma(\boldsymbol{y})\,\mathrm{d}s(\boldsymbol{y}) \quad (\boldsymbol{x} \in \mathbb{R}^2),\ S_\alpha\sigma(\boldsymbol{x}) := \int_\Gamma G_\alpha(\boldsymbol{x}, \boldsymbol{y})\sigma(\boldsymbol{y})\,\mathrm{d}s(\boldsymbol{y}) \quad (\boldsymbol{x} \in \Gamma), \tag{30}$$

and the *complex-scaled NP operator* is

$$K^\star_\alpha\sigma(\boldsymbol{x}) := \mathrm{pv}\int_\Gamma \partial_{\alpha\nu(\boldsymbol{x})} G_\alpha(\boldsymbol{x}, \boldsymbol{y})\sigma(\boldsymbol{y})\,\mathrm{d}s(\boldsymbol{y}) \quad (\boldsymbol{x} \in \Gamma). \tag{31}$$

In the study of the above complex-scaled operators, there is a technical difficulty that we would like to emphasize here, although it is not significant for numerical applications. The Sobolev mapping properties of BI operators associated with strongly elliptic equations, recalled in Appendix A, require the coefficients to be smooth; hence they do not apply to $\mathcal{P}_\alpha$. The main difficulty is not the jump discontinuity of A_α across ∂B_α but the fact that A_α is not continuous at $\boldsymbol{x_c}$. However, since A_α is not singular at $\boldsymbol{x_c}$ we do not expect this feature to influence the regularity of the BI operators; we capture this expectation in the following conjecture.

Conjecture 17. *When $\Re(\alpha) > 0$, Propositions 26, 27, and 31 apply to $\mathcal{P}_\alpha$.*

In particular, we consider that $\mathcal{S}_\alpha : H^{-1/2}(\Gamma) \to H^1_{\alpha,\mathrm{loc}}(\mathbb{R}^2)$, $K^\star_\alpha \in \mathcal{B}(H^{-1/2}(\Gamma), H^{-1/2}(\Gamma))$, and that the jump relations

$$[\![\mathcal{S}_\alpha\sigma]\!]_\Gamma = 0, \;\; \partial^\pm_{\alpha\nu}\mathcal{S}_\alpha\sigma = K^\star_\alpha\sigma \mp \frac{1}{2}\sigma,$$

take place in $H^{1/2}(\Gamma)$ and $H^{-1/2}(\Gamma)$, respectively. The relevance of $K^\star_\alpha$ for our purposes is covered next.

3.4. Essential spectrum of the complex-scaled NP operator

Our interest is in the following complex-scaled eigenvalue problem.

Definition 18 (Complex-scaled NP eigenvalue problem)**.** Find $(\sigma_\alpha, \lambda) \in H^{-1/2}(\Gamma) \times \mathbb{C}\backslash\{-1/2\}$, $\sigma_\alpha \neq 0$, such that

$$K^\star_\alpha[\sigma_\alpha](\boldsymbol{x}) = \lambda\,\sigma_\alpha(\boldsymbol{x}) \quad (\boldsymbol{x} \in \Gamma). \tag{32}$$

Reasoning identically to Section 2.2, the equivalence between (24) and (32) combined with the corner expansion of Proposition 15 suggests that the essential spectrum of $K^\star_\alpha$ is

$$\sigma_{\mathrm{ess}}(K^\star_\alpha) = \bigcup_{\rho\in\{\mathfrak{e},\mathfrak{v}\}} \sigma^\rho_{\mathrm{ess}}(K^\star_\alpha), \;\; \sigma^\rho_{\mathrm{ess}}(K^\star_\alpha) = \overline{\{\lambda \in \mathbb{C} \mid \exists\eta \in \mathbb{R}^* : \; g^\rho(\alpha\eta, \lambda) = 0\}}. \tag{33}$$

This set is plotted in Figure 5 for different values of $\arg(\alpha)$, the modulus of α having no influence. This plot, which is similar to [11, Fig. 7], illustrates that complex scaling moves the essential spectrum away from the real axis, implying that $K^\star_\alpha$ is not similar to a self-adjoint operator anymore. Specifically, as $\arg(\alpha)$ is increased, $\sigma_{\mathrm{ess}}(K^\star_\alpha)$ deforms while staying attached at its two end points $\pm\lambda_c(\phi)$ and 0, with a spiraling behavior around 0.

The open subset of $\mathbb{C}$ covered by the movement of the essential spectrum, shaded in Figure 5, is known in complex-scaling parlance as the *uncovered region* U_α. The following properties, which can be deduced from [11, Prop. 22], are the most important in practice:

1. The complex (resp. real) eigenvalues of $K^\star_\alpha$ that lie inside U_α (resp. $\overline{U}_\alpha \cap \mathbb{R}$) are complex resonances (resp. embedded eigenvalues) of $K^\star$.
2. The real eigenvalues of $K^\star_\alpha$ that lie outside $\overline{U_\alpha}$ are isolated eigenvalues of $K^\star$.

However, before we can discretize (32) we need a closed-form expression of the complex-scaled Green's function G_α: this is the purpose of the next section.

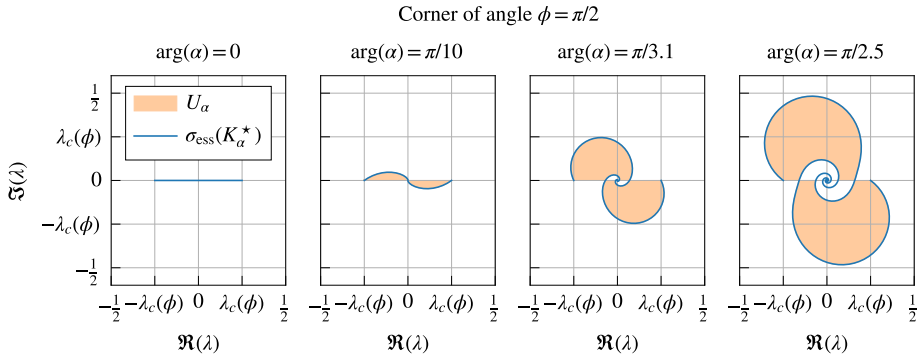

Figure 5: Essential spectrum of complex-scaled NP operator (33) and uncovered region for increasing values of $\arg(\alpha)$.

4. Complex-scaled Green's function

The purpose of this section is to obtain a closed-form expression of the complex-scaled Green's function, i.e. to solve (29), which will enable us to compute the complex-scaled layer potentials and BI operators introduced in Section 3. The derivation of G_α proceeds in two steps. In Section 4.1 we obtain a function that solves (29) only when $\boldsymbol{y} \notin \overline{B_\alpha}$. An extension that can handle the case $\boldsymbol{y} \in \overline{B_\alpha}$ is obtained in Section 4.2, which turns out to require some elementary albeit tedious computations. For clarity, we assume that $N_c = 1$ and we will refer to results in Appendix B for some computations.

4.1. Partial expression of the Green's function

Let us introduce the analytic continuation of the Green's function (2):

$$\hat{G}(\boldsymbol{x}, \boldsymbol{y}) := -\frac{1}{4\pi} \ln q_1(\boldsymbol{x}, \boldsymbol{y}), \;\; q_1(\boldsymbol{x}, \boldsymbol{y}) := \sum_{i=1}^{2} (x_i - y_i)^2,$$

where $\boldsymbol{x}, \boldsymbol{y} \in \mathbb{C}^2$ and ln is the principal branch of the logarithm with branch cut on $(-\infty, 0)$. Previous works involving BIEs with (linear) complex scaling [12, 13] suggest introducing

$$\mathfrak{G}_\alpha(\boldsymbol{x}, \boldsymbol{y}) := -\frac{1}{4\pi} \ln q_\alpha(\boldsymbol{x}, \boldsymbol{y}),$$

where q_α is the complex-scaled squared Euclidian distance

$$q_\alpha(\boldsymbol{x}, \boldsymbol{y}) := q_1(\Gamma_\alpha(\boldsymbol{x}), \Gamma_\alpha(\boldsymbol{y})) = \sum_{i=1}^{2} (\gamma_i(\boldsymbol{x}) - \gamma_i(\boldsymbol{y}))^2.$$

Our objective is to verify wether $\mathfrak{G}_\alpha$ solves (29) when $\Re(\alpha) > 0$. The next two results establish the domain of definition and regularity of $\mathfrak{G}_\alpha$; for convenience we introduce the notation

$$\mathring{\mathbb{R}}^4 := \{(\boldsymbol{x}, \boldsymbol{y}) \in \mathbb{R}^2 \times \mathbb{R}^2 \,|\, \boldsymbol{x} \neq \boldsymbol{y}\}, \;\; \mathbb{R}^2_\alpha := \mathbb{R}^2 \backslash \overline{B_\alpha}.$$

Lemma 19. *When $\Re(\alpha) > 0$, $\mathfrak{G}_\alpha \in C^0(\mathring{\mathbb{R}}^4 \backslash B_\alpha^2) \cap C^\infty(\mathring{\mathbb{R}}^4 \backslash \overline{B_\alpha^2})$ with strong gradients given by*

$$\nabla_{\boldsymbol{x}} \mathfrak{G}_\alpha(\boldsymbol{x}, \boldsymbol{y}) = -\frac{J_\alpha(\boldsymbol{x})}{2\pi} \frac{\Gamma_\alpha(\boldsymbol{x}) - \Gamma_\alpha(\boldsymbol{y})}{q_\alpha(\boldsymbol{x}, \boldsymbol{y})}, \quad \nabla_{\boldsymbol{y}} \mathfrak{G}_\alpha(\boldsymbol{x}, \boldsymbol{y}) = \frac{J_\alpha(\boldsymbol{y})}{2\pi} \frac{\Gamma_\alpha(\boldsymbol{x}) - \Gamma_\alpha(\boldsymbol{y})}{q_\alpha(\boldsymbol{x}, \boldsymbol{y})}.$$

Moreover, for any $(\boldsymbol{x}, \boldsymbol{y}) \in \mathbb{R}^4$, $\nabla_x \mathfrak{G}_\alpha(\cdot, \boldsymbol{y})$ and $\nabla_y \mathfrak{G}_\alpha(x, \cdot)$ belong to $L^1_{\mathrm{loc}}(\mathbb{R}^2)$.

Proof. The continuity claim follows from Lemma 32, which implies that $\mathfrak{G}_\alpha$ is well-defined and continuous on $\mathring{\mathbb{R}}^4 \backslash B_\alpha^2$ since it does not involve logarithms of negative or null quantities. Then, the smoothness and the gradients follows from Lemma 11 and the chain rule. The claim that the strong gradients are locally integrable is a consequence of Lemma 38. □

Lemma 20. *Let $\Re(\alpha) > 0$ and $\gamma \in (0, 1)$. For any compact sets $U_1 \subset \mathbb{R}^2$ and $U_2 \subset \mathbb{R}^2_\alpha$, there is a constant $C > 0$ such that*

$$\forall (\boldsymbol{x}, \boldsymbol{y}) \in U_1 \times U_2 : \boldsymbol{x} \neq \boldsymbol{y}, \ |\mathfrak{G}_\alpha(\boldsymbol{x}, \boldsymbol{y})| \leq \frac{C}{|\boldsymbol{x} - \boldsymbol{y}|^\gamma}.$$

Proof. From Lemma 19, $\ln q_\alpha \in C^0([U_1 \times U_2] \cap \mathring{\mathbb{R}}^4)$ so that to establish the claim it remains to investigate the case $|\boldsymbol{x} - \boldsymbol{y}| \to 0$. But here this is straightforward since for any $(\boldsymbol{x}, \boldsymbol{y}) \in \mathbb{R}^2_\alpha$, $q_\alpha(\boldsymbol{x}, \boldsymbol{y}) = |\boldsymbol{x} - \boldsymbol{y}|^2$, so that $(\boldsymbol{x}, \boldsymbol{y}) \mapsto |\boldsymbol{x} - \boldsymbol{y}|^\gamma q_\alpha(\boldsymbol{x}, \boldsymbol{y}) \in C^0(U_1 \times U_2)$ for any $\gamma > 0$. □

We are now in a position to verify that $\mathfrak{G}_\alpha$ is the free space Green's function of $\mathcal{P}_\alpha$, but only when $\boldsymbol{x}$ and $\boldsymbol{y}$ are not both in the scaling region.

Proposition 21. *Let $\Re(\alpha) > 0$. For any $\boldsymbol{y} \in \mathbb{R}^2_\alpha$, $\mathfrak{G}_\alpha(\cdot, \boldsymbol{y})$ solves*

$$-\nabla_x \cdot [A_\alpha(\boldsymbol{x}) \nabla_x \mathfrak{G}_\alpha(\boldsymbol{x}, \boldsymbol{y})] = \delta(\boldsymbol{x} - \boldsymbol{y}) \quad (\boldsymbol{x} \in \mathbb{R}^2).$$

Proof. Let $\boldsymbol{y} \in \mathbb{R}^2_\alpha$ and $\varphi \in C_c^\infty(\mathbb{R}^2)$. Using Lemmas 19 and 20, we deduce that both $\mathfrak{G}_\alpha(\cdot, \boldsymbol{y})$ and its *weak* gradient belong to $L^1_{\mathrm{loc}}(\mathbb{R}^2)$. Since $A_\alpha \in L^\infty(\mathbb{R}^2)$ from Proposition 14, we have $A_\alpha \nabla_x \mathfrak{G}_\alpha(\cdot, \boldsymbol{y}) \in L^1_{\mathrm{loc}}(\mathbb{R}^2)$. To show the claim, it remains to compute the weak divergence of $A_\alpha \nabla_x \mathfrak{G}_\alpha(\cdot, \boldsymbol{y})$, which is by definition

$$\begin{aligned} \langle \nabla_x \cdot [A_\alpha \nabla_x \mathfrak{G}_\alpha(\cdot, \boldsymbol{y})], \varphi \rangle &:= -\int_{\mathbb{R}^2} A_\alpha(\boldsymbol{x}) \nabla_x \mathfrak{G}_\alpha(\boldsymbol{x}, \boldsymbol{y}) \cdot \nabla \varphi(\boldsymbol{x}) \, \mathrm{d}\boldsymbol{x}. \\ &= -\lim_{\varepsilon \to 0} \int_{\mathbb{R}^2 \backslash [B(\boldsymbol{x_c}, \varepsilon) \cup B(\boldsymbol{y}, \varepsilon)]} A_\alpha(\boldsymbol{x}) \nabla_x \mathfrak{G}_\alpha(\boldsymbol{x}, \boldsymbol{y}) \cdot \nabla \varphi(\boldsymbol{x}) \, \mathrm{d}\boldsymbol{x} = \lim_{\varepsilon \to 0} I(\varepsilon). \end{aligned}$$

The first Green's identity in $B_\alpha \backslash [B(\boldsymbol{x_c}, \varepsilon) \cup B(\boldsymbol{y}, \varepsilon)]$ and $\mathbb{R}^2_\alpha \backslash B(\boldsymbol{y}, \varepsilon)$ gives

$$\begin{aligned} I(\varepsilon) = &\int_{\partial B(\boldsymbol{y}, \varepsilon)} A_\alpha(\boldsymbol{x}) \nabla_x \mathfrak{G}_\alpha(\boldsymbol{x}, \boldsymbol{y}) \cdot \boldsymbol{\nu}(\boldsymbol{x}) \varphi(\boldsymbol{x}) \, \mathrm{d}s(\boldsymbol{x}) \\ &+ \int_{\partial B(\boldsymbol{x_c}, \varepsilon)} A_\alpha(\boldsymbol{x}) \nabla_x \mathfrak{G}_\alpha(\boldsymbol{x}, \boldsymbol{y}) \cdot \boldsymbol{\nu}(\boldsymbol{x}) \varphi(\boldsymbol{x}) \, \mathrm{d}s(\boldsymbol{x}) \\ &+ \int_{\partial B_\alpha} [\![A_\alpha(\boldsymbol{x}) \nabla_x \mathfrak{G}_\alpha(\boldsymbol{x}, \boldsymbol{y})]\!] \cdot \boldsymbol{\nu}(\boldsymbol{x}) \varphi(\boldsymbol{x}) \, \mathrm{d}s(\boldsymbol{x}) \\ &+ \int_{\mathbb{R}^2 \backslash [B(\boldsymbol{x_c}, \varepsilon) \cup B(\boldsymbol{y}, \varepsilon)]} \nabla_x \cdot [A_\alpha(\boldsymbol{x}) \nabla_x \mathfrak{G}_\alpha(\boldsymbol{x}, \boldsymbol{y})] \varphi(\boldsymbol{x}) \, \mathrm{d}s(\boldsymbol{x}). \end{aligned}$$

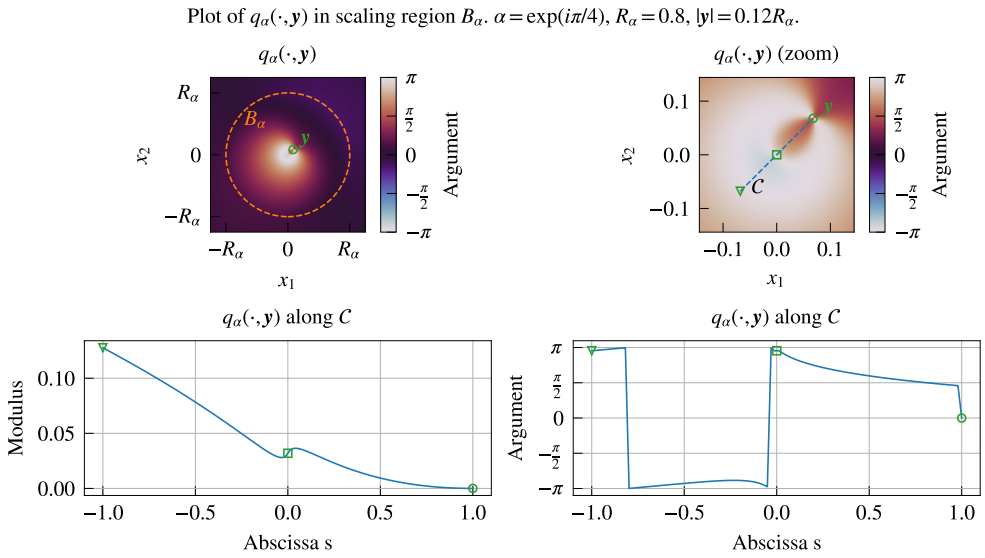

Figure 6: Plot of $\boldsymbol{x} \mapsto q_\alpha(\boldsymbol{x},\boldsymbol{y})$ for a given $\boldsymbol{y} \in B_\alpha$ with $\boldsymbol{x_c} = (0,0)$. (Top) Principal argument in B_α. (Bottom) Modulus and principal argument along the curve C.

Let us examine each term on the right-hand side, starting from the top. (i) Tends to $-\varphi(\boldsymbol{y})$ from Lemma 42. (ii) Tends to zero from Lemma 39. (iii) The jump term can be rewritten as $[\![A_\alpha \nabla_x \mathfrak{G}_\alpha]\!] \cdot \boldsymbol{\nu}(\boldsymbol{x}) = \nabla_x \hat{G}(\Gamma_\alpha(\boldsymbol{x}),\Gamma_\alpha(\boldsymbol{y})) \cdot [\![J_\alpha A_\alpha \boldsymbol{\nu}]\!]$, which is null from Lemma 37. (iv) Null by construction of $\mathfrak{G}_\alpha$. □

The next section deals with the case where both $\boldsymbol{x}$ and $\boldsymbol{y}$ are in the scaling region.

4.2. Complete expression of the Green's function

The function $\mathfrak{G}_\alpha$ is not continuous over $\mathring{\mathbb{R}}^4 \cap B_\alpha^2$ due to q_α crossing the branch cut of ln, so that it does not solve (29) for $\boldsymbol{y} \in B_\alpha$. In this section we derive a continuous extension of $\mathfrak{G}_\alpha$ to $\mathring{\mathbb{R}}^4 \cap B_\alpha^2$ using only the principal branch of the logarithm, and check that it does solves (29) for any $\boldsymbol{y} \in \mathbb{R}^2$. Before introducing the expression of our continuous extension, let us illustrate what is happening. In the case $\boldsymbol{y} = \boldsymbol{x_c}$, the quantity q_α simplifies to

$$q_\alpha(\boldsymbol{x},\boldsymbol{x_c}) = R_\alpha^2 \exp\left[\frac{2}{\hat{\alpha}(\boldsymbol{x})} \ln\left(\frac{|\boldsymbol{x}-\boldsymbol{x_c}|}{R_\alpha}\right)\right] \quad (\boldsymbol{x} \neq \boldsymbol{x_c}).$$

When $\boldsymbol{x} \notin B_\alpha$, from Lemma 32 the quantity $\ln q_\alpha(\boldsymbol{x},\boldsymbol{x_c})$ is well-defined. By contrast, as $\boldsymbol{x} \to \boldsymbol{x_c}$, $q_\alpha(\boldsymbol{x},\boldsymbol{x_c})$ crosses the branch cut of ln infinitely many times when $\alpha \notin \mathbb{R}$ since

$$\arg q_\alpha(\boldsymbol{x},\boldsymbol{x_c}) = \Im\left(\frac{2}{\hat{\alpha}(\boldsymbol{x})}\right) \ln\left(\frac{|\boldsymbol{x}-\boldsymbol{x_c}|}{R_\alpha}\right) \pmod{2\pi},$$

so that "$\ln q_\alpha(\cdot,\boldsymbol{x_c})$" is discontinuous inside B_α (see Figure 4). However, here the way out is straightforward since the map

$$\mathbb{R}^2 \backslash \{\boldsymbol{x_c}\} \to \mathbb{C}, \ \boldsymbol{x} \mapsto \ln(R_\alpha^2) + \frac{2}{\hat{\alpha}(\boldsymbol{x})} \ln\left(\frac{|\boldsymbol{x}-\boldsymbol{x_c}|}{R_\alpha}\right)$$

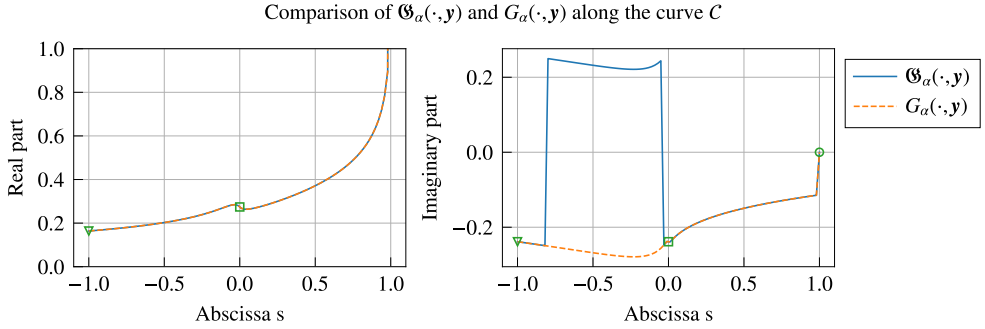

Figure 7: Comparison of $\boldsymbol{x} \mapsto \mathfrak{G}_\alpha(\boldsymbol{x}, \boldsymbol{y})$ and $\boldsymbol{x} \mapsto G_\alpha(\boldsymbol{x}, \boldsymbol{y})$ for a given $\boldsymbol{y} \in B_\alpha$ with $\boldsymbol{x_c} = (0, 0)$. The values are taken along the curve C shown in Figure 6.

is continuous and coincides with $\ln q_\alpha(\cdot, \boldsymbol{x_c})$ over $\mathbb{R}^2 \backslash B_\alpha$.

When $\boldsymbol{y} \neq \boldsymbol{x_c}$, the exact same phenomenon occurs; since this is more difficult to see analytically we illustrate it in Figure 6, which plots the modulus and argument of $\boldsymbol{x} \mapsto q_\alpha(\boldsymbol{x}, \boldsymbol{y})$ for a given $\boldsymbol{y}$ inside B_α. The plot shows that as $\boldsymbol{x}$ travels along the line C, q_α crosses the real negative axis: the corresponding jump discontinuity in the imaginary part of $\mathfrak{G}_\alpha$ is plotted in Figure 7.

In our experience, this discontinuity is not a significant computational issue when evaluating the complex-scaled single-layer potential (30) since it occurs close to the corner where, thanks to the complex scaling, the density vanishes. However, for the sake of completeness, we now derive a closed-form expression of the complete Green's function.

The above analysis of the case $\boldsymbol{y} = \boldsymbol{x_c}$ suggests that it may be possible to extend continuously $\ln q_\alpha$ from $\mathring{\mathbb{R}}^4 \backslash B_\alpha^2$ to $\mathring{\mathbb{R}}^4 \cap B_\alpha^2$ by factoring out a well-chosen exponential term. This motivates the introduction of the factorization

$$\forall (\boldsymbol{x}, \boldsymbol{y}) \in \mathring{\mathbb{R}}^4, \; q_\alpha(\boldsymbol{x}, \boldsymbol{y}) = \begin{cases} \exp\left[\frac{2}{\tilde{\alpha}(\boldsymbol{x})} \ln\left(\frac{|\boldsymbol{x}-\boldsymbol{x_c}|}{R_\alpha}\right)\right] \times \hat{q}_\alpha(\boldsymbol{x}, \boldsymbol{y}) & (|\boldsymbol{y}-\boldsymbol{x_c}| \leq |\boldsymbol{x}-\boldsymbol{x_c}|) \\ \exp\left[\frac{2}{\tilde{\alpha}(\boldsymbol{y})} \ln\left(\frac{|\boldsymbol{y}-\boldsymbol{x_c}|}{R_\alpha}\right)\right] \times \hat{q}_\alpha(\boldsymbol{y}, \boldsymbol{x}) & (|\boldsymbol{x}-\boldsymbol{x_c}| \leq |\boldsymbol{y}-\boldsymbol{x_c}|), \end{cases}$$

where

$$\hat{q}_\alpha(\boldsymbol{x}, \boldsymbol{y}) := \frac{q_\alpha(\boldsymbol{x}, \boldsymbol{y})}{\exp\left[\frac{2}{\tilde{\alpha}(\boldsymbol{x})} \ln\left(\frac{|\boldsymbol{x}-\boldsymbol{x_c}|}{R_\alpha}\right)\right]} \quad (\boldsymbol{x} \neq \boldsymbol{x_c}),$$

and the candidate Green's function

$$G_\alpha(\boldsymbol{x}, \boldsymbol{y}) := \begin{cases} \mathfrak{G}_\alpha(\boldsymbol{x}, \boldsymbol{y}) & ((\boldsymbol{x}, \boldsymbol{y}) \notin B_\alpha^2) \\ -\frac{1}{2\pi\alpha} \ln \frac{|\boldsymbol{x}-\boldsymbol{x_c}|}{R_\alpha} - \frac{1}{4\pi} \ln \hat{q}_\alpha(\boldsymbol{x}, \boldsymbol{y}) & (|\boldsymbol{y}-\boldsymbol{x_c}| \leq |\boldsymbol{x}-\boldsymbol{x_c}| < R_\alpha) \\ -\frac{1}{2\pi\alpha} \ln \frac{|\boldsymbol{y}-\boldsymbol{x_c}|}{R_\alpha} - \frac{1}{4\pi} \ln \hat{q}_\alpha(\boldsymbol{y}, \boldsymbol{x}) & (|\boldsymbol{x}-\boldsymbol{x_c}| < |\boldsymbol{y}-\boldsymbol{x_c}| < R_\alpha), \end{cases} \tag{34}$$

whose regularity is illustrated in Figure 7 and established by the next result.

Proposition 22. *Let $\Re(\alpha) > 0$. The function G_α given by (34) satisfies:*

1. $G_\alpha \in C^0(\mathring{\mathbb{R}}^4)$,

2. *G_α is infinitely smooth almost everywhere, with strong gradients identical to those of $\mathfrak{G}_\alpha$:*

$$\nabla_{\boldsymbol{x}} G_\alpha(\boldsymbol{x},\boldsymbol{y}) = -\frac{J_\alpha(\boldsymbol{x})}{2\pi}\frac{\Gamma_\alpha(\boldsymbol{x})-\Gamma_\alpha(\boldsymbol{y})}{q_\alpha(\boldsymbol{x},\boldsymbol{y})},\ \nabla_{\boldsymbol{y}} G_\alpha(\boldsymbol{x},\boldsymbol{y}) = \frac{J_\alpha(\boldsymbol{y})}{2\pi}\frac{\Gamma_\alpha(\boldsymbol{x})-\Gamma_\alpha(\boldsymbol{y})}{q_\alpha(\boldsymbol{x},\boldsymbol{y})}.$$

3. *For any $\gamma \in (0,1)$ and compact sets $U_1, U_2 \subset \mathbb{R}^2$, there is a constant $C > 0$ such that*

$$\forall (\boldsymbol{x},\boldsymbol{y}) \in U_1 \times U_2 :\ \boldsymbol{x} \neq \boldsymbol{y},\ |G_\alpha(\boldsymbol{x},\boldsymbol{y})| \leq \frac{C}{|\boldsymbol{x}-\boldsymbol{y}|^\gamma}.$$

Proof.

1. Lemma 33 implies that the map

$$(\boldsymbol{x},\boldsymbol{y}) \mapsto \ln \hat{q}_\alpha(\boldsymbol{x},\boldsymbol{y}) \quad (|\boldsymbol{y}-\boldsymbol{x}_c| \leq |\boldsymbol{x}-\boldsymbol{x}_c|,\ \boldsymbol{x} \neq \boldsymbol{y}),$$

is well-defined and continuous since $\hat{q}_\alpha$ never crosses the branch cut of ln. Combined with Lemma 19, this ensures that the three functions on the right-hand side of (34) are well-defined and continuous on their domains of definitions. Hence, to prove continuity it remains to check that they match. (i) When $|\boldsymbol{x}-\boldsymbol{x}_c| = |\boldsymbol{y}-\boldsymbol{x}_c| \leq R_\alpha$,

$$\ln(|\boldsymbol{x}-\boldsymbol{x}_c|/R_\alpha) = \ln(|\boldsymbol{y}-\boldsymbol{x}_c|/R_\alpha) \text{ and } \hat{q}_\alpha(\boldsymbol{x},\boldsymbol{y}) = \hat{q}_\alpha(\boldsymbol{y},\boldsymbol{x}),$$

so that the bottom two functions in the right-hand side of (34) match. (ii) For any $(\boldsymbol{x},\boldsymbol{y}) \in \partial B_\alpha^2$,

$$\ln(|\boldsymbol{x}-\boldsymbol{x}_c|/R_\alpha) = 0 \text{ and } \hat{q}_\alpha(\boldsymbol{x},\boldsymbol{y}) \overset{\text{Lemma 33}}{=} q_\alpha(\boldsymbol{x},\boldsymbol{y}),$$

so that the top and middle functions in the right-hand side of (34) match.

2. The three functions in the right-hand side of (34) are continuously differentiable and computing their strong gradient using the chain rule gives the claim. Alternatively, this can also be deduced from the fact that branches of the logarithm differ by an additive constant.
3. Since G_α is continuous on $\mathring{\mathbb{R}}^4$, the claim follows from the fact that the singularity as $\boldsymbol{x} \to \boldsymbol{y}$ is at most logarithmic (this is the same argument as in the proof of Lemma 20).

□

So far, we have extended $\mathfrak{G}_\alpha$ continuously to $\mathring{\mathbb{R}}^4 \cap B_\alpha^2$ using only the principal branch of the logarithm; we can now check that G_α is the sought Green's function.

Proposition 23. *Let $\Re(\alpha) > 0$. For any $\boldsymbol{y} \in \mathbb{R}^2$, the function $G_\alpha(\cdot,\boldsymbol{y})$ given by (34) solves (29).*

Proof. Let $\boldsymbol{y} \in \mathbb{R}^2$ and $\varphi \in C_c^\infty(\mathbb{R}^2)$. From Proposition 22 and Lemma 38, we deduce that both $G_\alpha(\cdot,\boldsymbol{y})$ and its *weak* gradient belong to $L^1_{\mathrm{loc}}(\mathbb{R}^2)$. The proof is then identical to that of Proposition 21, since Lemmas 39 and 42 apply for any $\boldsymbol{y} \in \mathbb{R}^2$. □

For reference, we end this section with a simplified expression of $K_\alpha^\star$.

Lemma 24. *Let $\Re(\alpha) > 0$. The complex-scaled NP operator (31) and its adjoint satisfy*

$$K_\alpha^\star \sigma(\boldsymbol{x}) = \frac{-1}{2\pi}\mathrm{pv}\int_\Gamma \frac{\mu_\alpha(\boldsymbol{x})}{\hat{\alpha}(\boldsymbol{x})}\frac{(\Gamma_\alpha(\boldsymbol{x})-\Gamma_\alpha(\boldsymbol{y}))\cdot\boldsymbol{\nu}(\boldsymbol{x})}{q_\alpha(\boldsymbol{x},\boldsymbol{y})}\sigma(\boldsymbol{y})\,\mathrm{d}s(\boldsymbol{y}) \quad (\boldsymbol{x} \in \Gamma) \tag{35}$$

$$K_\alpha \sigma(\boldsymbol{x}) = \frac{1}{2\pi}\mathrm{pv}\int_\Gamma \frac{\mu_\alpha(\boldsymbol{y})}{\hat{\alpha}(\boldsymbol{y})}\frac{(\Gamma_\alpha(\boldsymbol{x})-\Gamma_\alpha(\boldsymbol{y}))\cdot\boldsymbol{\nu}(\boldsymbol{x})}{q_\alpha(\boldsymbol{x},\boldsymbol{y})}\sigma(\boldsymbol{y})\,\mathrm{d}s(\boldsymbol{y}) \quad (\boldsymbol{x} \in \Gamma).$$

Proof. Let $\boldsymbol{x} \in \Gamma$ such that $\boldsymbol{x} \neq \boldsymbol{x_c}$ and $\boldsymbol{x} \notin \partial B_\alpha$. Using $A_\alpha^T = A_\alpha$, $J_\alpha^T = J_\alpha$, and Lemma 35 we can express the conormal derivative as

$$\partial_{\alpha\nu(\boldsymbol{x})} G_\alpha(\boldsymbol{x}, \boldsymbol{y}) = -\frac{1}{2\pi} \frac{\Gamma_\alpha(\boldsymbol{x}) - \Gamma_\alpha(\boldsymbol{y})}{q_\alpha(\boldsymbol{x}, \boldsymbol{y})} \cdot \left(\frac{\mu_\alpha(\boldsymbol{x})}{\hat{\alpha}(\boldsymbol{x})} \left[I + (\hat{\alpha}(\boldsymbol{x}) - 1) P_c(\boldsymbol{x}) \right] \boldsymbol{\nu}(\boldsymbol{x}) \right),$$

where the term involving the projection matrix P_c is null. Indeed, if $\boldsymbol{x} \notin \overline{B_\alpha}$, then $\hat{\alpha}(\boldsymbol{x}) = 1$, and if $\boldsymbol{x} \in B_\alpha$, then $(\boldsymbol{x} - \boldsymbol{x_c}) \cdot \boldsymbol{\nu}(\boldsymbol{x}) = 0$ since from Assumption 1 corners are straight. □

Equipped with a way to evaluate the complex-scaled Green function's, we proceed to numerical computations in Section 5.

Remark 25. Using Assumption 1, we find the usual formula: [48, (13.1.34)]

$$\forall \boldsymbol{x} \in \mathbb{R}^2 \backslash \{\boldsymbol{x_c}\}, \ \lim_{\boldsymbol{y} \to \boldsymbol{x}} \frac{(\Gamma_\alpha(\boldsymbol{x}) - \Gamma_\alpha(\boldsymbol{y})) \cdot \boldsymbol{\nu}(\boldsymbol{x})}{q_\alpha(\boldsymbol{x}, \boldsymbol{y})} = \begin{cases} \kappa_c(\boldsymbol{x})/2 & (\boldsymbol{x} \notin B_\alpha) \\ 0 & (\boldsymbol{x} \in B_\alpha), \end{cases}$$

where $\kappa_c(\boldsymbol{x})$ is the signed curvature of Γ.

5. Numerical results

This section focuses on the discretization of the complex-scaled NP operator $K_\alpha^\star$ and gathers the numerical results[6] obtained by solving the eigenvalue problem (32). Section 5.1 describes the employed Nyström method, which is validated in the next two sections. Section 5.2 considers an ellipse, which has only point spectrum, while Section 5.3 considers a corner geometry, which has only essential spectrum. Sections 5.4 and 5.5 then demonstrate that $K_\alpha^\star$ can be used to compute embedded eigenvalues and complex resonances by considering corner perturbations of an ellipse as well as a geometry from [49].

5.1. Nyström discretization method

The continuous boundary Γ is approximated by a discrete boundary Γ^h that is a union of N non-overlapping elements

$$\Gamma^h = \bigcup_{n=1}^{N} \Gamma_n^h,$$

where $h > 0$ is the maximum element size (the smaller h the larger N). Each element Γ_n^h is mapped from the reference element $[-1, 1]$ through the vector-valued map $\varphi_n^h : [-1, 1] \to \Gamma_n^h \subset \mathbb{R}^2$. In the presented numerical applications Γ^h is given by a second-order mesh generated with gmsh [50], so that each component of φ_n^h is a polynomial of degree 2. To integrate over Γ^h we use a composite quadrature rule

$$Q^h = \bigcup_{n=1}^{N} \bigcup_{p=1}^{P} \{(\boldsymbol{x_{p,n}^h}, w_{p,n}^h)\}$$

obtained from the Gauss-Legendre quadrature rule on the reference element $(\hat{x}_p, \hat{w}_p)_{1 \leq p \leq P}$. This quadrature rule is exact for polynomials of degree $2P - 1$.

[6] Code available at https://doi.org/10.5281/zenodo.16309756.

In order to describe the discretization method, let us consider the potential

$$\mathcal{T}\sigma(\boldsymbol{x}) = \int_\Gamma k(\boldsymbol{x},\boldsymbol{y})\sigma(\boldsymbol{y})\,\mathrm{d}s(\boldsymbol{y}) \quad (\boldsymbol{x}\in\mathbb{R}^2),$$

where k is a weakly singular kernel [3, § 2.3]. To evaluate this potential, we use a Nyström method combined with a product integration method to handle nearly and weakly singular terms [51, Chap. 4]. The corresponding discrete operator is

$$\mathcal{T}^h\sigma(\boldsymbol{x}) \coloneqq \sum_{m=1}^{N}\sum_{j=1}^{P} \mathcal{T}^h_{j,m}(\boldsymbol{x})\sigma(\boldsymbol{x}^{\boldsymbol{h}}_{\boldsymbol{j},\boldsymbol{m}}), \tag{36}$$

where the coefficients are

$$\mathcal{T}^h_{j,m}(\boldsymbol{x}) \coloneqq \begin{cases} k(\boldsymbol{x},\boldsymbol{x}^{\boldsymbol{h}}_{\boldsymbol{j},\boldsymbol{m}})w^h_{j,m} & \text{if } \operatorname{dist}(\boldsymbol{x},\Gamma^h_m) > \delta_d \\ \int_{\Gamma^h_m} k(\boldsymbol{x},\boldsymbol{y})l^h_{j,m}(\boldsymbol{y})\,\mathrm{d}s(\boldsymbol{y}) & \text{otherwise,} \end{cases} \tag{37}$$

with $\delta_d > 0$ a parameter and $l^h_{i,n} = \hat{l}_i \circ (\varphi^h_n)^{-1}$, where $(\hat{l}_i)_i$ is the Lagrange basis on the reference element

$$\hat{l}_i : [-1,1] \to \mathbb{R},\ \deg \hat{l}_i = P-1,\ \hat{l}_i(\hat{\boldsymbol{x}}_j) = \delta_{i,j}.$$

The integral in (37) is either nearly or weakly singular and we evaluate it using the Gauss-Legendre quadrature rule with $P_s > P$ nodes. We set $\delta_d = 10h$, unless mentioned otherwise. The number of quadrature nodes is set to $P = 2$ and $P_s = 6$; the presented results do not change sensibly when increasing P_s.

Let us now define our discrete operators. Since the complex-scaled single layer potential (30) is weakly singular, we can apply (36,37) with $k = G_\alpha$ to define $\mathcal{S}^h_\alpha\sigma(\boldsymbol{x})$ for any $\boldsymbol{x}\in\mathbb{R}^2$. The situation is more subtle for the complex-scaled NP operator (31): when $\boldsymbol{x} \neq \boldsymbol{x}^{\boldsymbol{k}}_{\boldsymbol{c}}$ (i.e. away from corners), $K^\star_\alpha\sigma(x)$ is well-defined as an improper integral and we can apply (36,37) with $k = \partial_{\alpha\nu(\boldsymbol{x})}G_\alpha$ to define $K^{\star,h}_\alpha\sigma(\boldsymbol{x})$. Since our quadrature points lie in the interior of each element Γ^h_n, we do not need to evaluate $K^\star_\alpha\sigma(\boldsymbol{x})$ at $\boldsymbol{x} = \boldsymbol{x}^{\boldsymbol{k}}_{\boldsymbol{c}}$. In summary, for a continuous density $\sigma\in C^0(\Gamma)$, $\mathcal{S}^h_\alpha\sigma(\boldsymbol{x})$ provides a pointwise approximation of $\mathcal{S}_\alpha\sigma(\boldsymbol{x})$ for any $\boldsymbol{x}\in\mathbb{R}^2$ while $K^{\star,h}_\alpha\sigma(\boldsymbol{x})$ provides a pointwise approximation of $K^\star_\alpha\sigma(\boldsymbol{x})$ only for $\boldsymbol{x}\in\Gamma\backslash\{\boldsymbol{x}^k_{\boldsymbol{c}}\}_k$.

Equipped with our discrete complex-scaled NP operator, we can discretize the eigenvalue problem (32) as the NP-dimensional linear eigenvalue problem: find $(\lambda^h,\sigma^h)\in\mathbb{C}\times\mathbb{C}^{NP}$ such that

$$\sum_{m=1}^{N}\sum_{j=1}^{P} K^{\star,h}_{\alpha,j,m}(\boldsymbol{x}^{\boldsymbol{h}}_{\boldsymbol{i},\boldsymbol{n}})\sigma^h_{j,m} = \lambda^h\sigma^h_{i,n} \quad (1\le i\le P, 1\le n\le N). \tag{38}$$

We will refer to NP as the number of degrees of freedom (DoF). The dense $NP\times NP$ matrix appearing in the left-hand side of (38) is real when $\alpha\in\mathbb{R}$ and complex when $\alpha\notin\mathbb{R}$; it is neither Hermitian nor normal. To solve (38) we use the QR method implemented in LAPACK through numpy [52]. Note that the same discretization method is used for the cases $\alpha = 1$ and $\alpha \neq 1$: the only difference lies in the expression of the Green's function, which is known analytically.

Let us end this section by emphasizing that there are many alternative discretization methods that can be applied to $K^\star_\alpha$, notably the modified Nyström methods [49, 53, 36, 54], which can deliver high accuracy for elliptic problems on domains with corners. However, the Nyström method presented in this section will prove sufficient for our purposes, which is the computation of embedded eigenvalues and complex resonances.

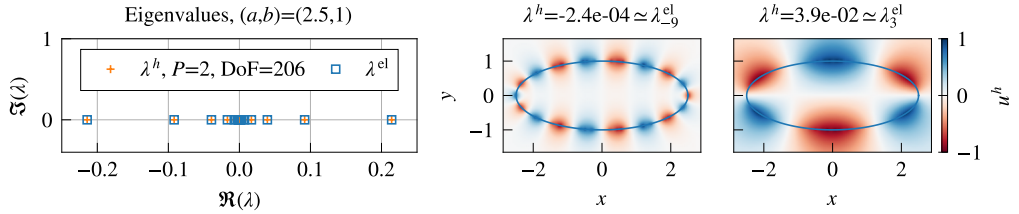

Figure 8: Discrete eigenvalue problem (38) for an ellipse. (Left) Computed and exact (39) eigenvalues. (Right) Computed eigenfunctions.

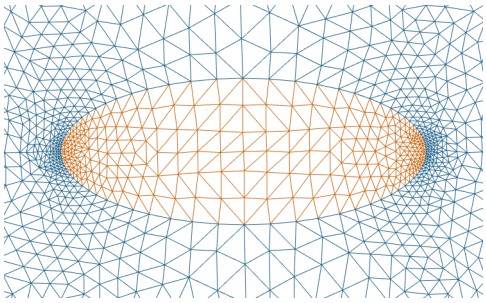

(a) Unstructured mesh.

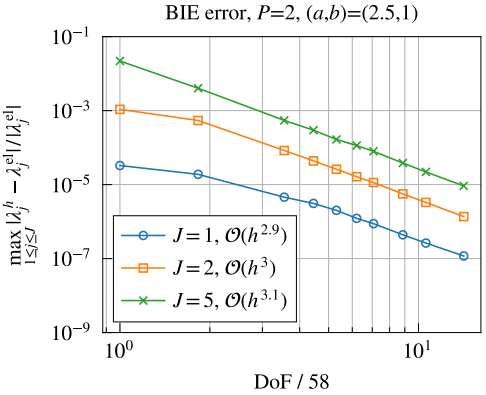

(b) Error obtained with Nyström method.

Figure 9: Discrete eigenvalue problem (38) for an ellipse with semi-axes (a, b).

5.2. *Validation: ellipse*

We consider an ellipse with semi-axes (a, b), for which eigenvalues are: [24, (4.13)]

$$\lambda_j^{\mathrm{el}} = \frac{\mathrm{sign}(j)}{2} \exp[-2|j| \operatorname{arctanh}(r)] \quad (j \in \mathbb{Z}^*), \tag{39}$$

where $r \in (0, 1)$ is the aspect ratio. Figure 8 plots the results obtained with the Nyström method described in Section 5.1 on a second-order unstructured mesh, an example of which is illustrated in Figure 9a. The eigenfunctions $u_n = \mathcal{S}[\sigma_n]$ are surface modes that are exponentially decaying away from Γ, a feature of all solutions of (5). Moreover, the smaller $|\lambda|$ the more localized and oscillatory u_n. Figure 9b plots the error and indicates the convergence rate estimated using a least squares fit on the last four points. It shows that we obtain the convergence rate

$$\max_{1 \le j \le J} \left| \lambda_j^h - \lambda_j^{\mathrm{el}} \right| \underset{h \to 0}{=} O(h^3),$$

which is optimal since the mesh is second order: increasing P does not improve the rate of convergence.

Figure 10 compares the Nyström method with a $\mathcal{P}^2$-Lagrange isoparametric FEM for (5), where the decay condition (5b) is enforced with the Dirichlet-to-Neumann operator on a circular boundary. To ensure a fair comparison, both methods rely on the same unstructured second-order mesh (ref. Figure 9a). Figure 10a illustrates that the FEM exhibits a spectral pollution

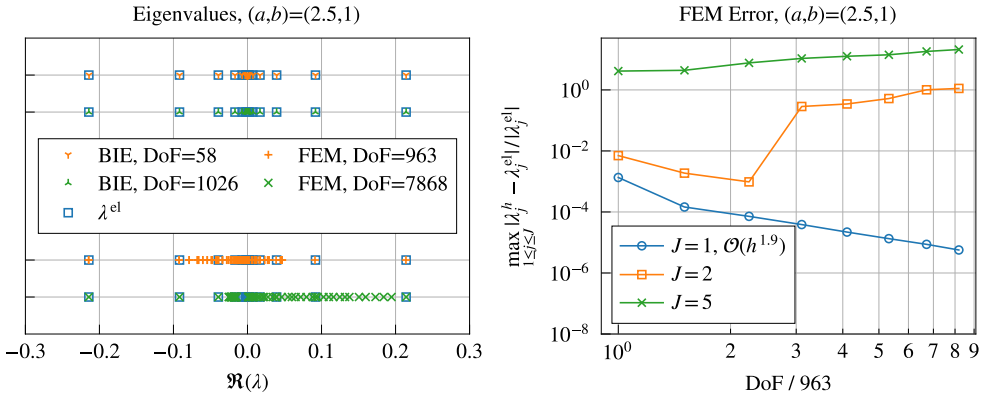

(a) Comparison with Nyström method.

(b) Error on largest eigenvalues.

Figure 10: Eigenvalue problem (5) for an ellipse, discretized with a $\mathcal{P}^2$-Lagrange isoparametric FEM.

around $\lambda = 0$ that spreads as the mesh is refined, thus preventing from accurately computing all eigenvalues. This pollution is further illustrated in the error plot of Figure 10b, which highlights that only the largest eigenvalue converges. This failure of the FEM is well-documented and can be fixed using a locally-symmetric mesh [33], which can be built analytically for an ellipse but is non-trivial to build for arbitrary curves. This elementary example shows the advantage of discretizing (4) instead of (5) to compute eigenvalues of smooth obstacles. We now turn to corners.

5.3. *Validation: corner*

Let Ω be the truncated corner of radius $R > 0$ and angle $\phi \in (0, 2\pi)\backslash\{\pi\}$:

$$\Omega = \{(r\cos\theta, r\sin\theta)\,|\,r \in [0, R),\ |\theta| < \phi/2\}\,,\ \Gamma = \partial\Omega,\ \Gamma_0 = \Gamma \cap \{r = R\}\,.$$

To validate the discretization of the complex-scaled NP operator $K_\alpha^\star$ when $\alpha \neq 1$, we consider the eigenvalue problem: find $(\sigma_\alpha, \lambda) \in H^{-1/2}(\Gamma) \times \mathbb{C}$, $\sigma_\alpha \neq 0$, such that

$$K_\alpha^\star[\sigma_\alpha](\boldsymbol{x}) = \lambda\sigma_\alpha(\boldsymbol{x}) \quad (\boldsymbol{x} \in \Gamma\backslash\Gamma_0),\ \mathcal{S}_\alpha[\sigma_\alpha](\boldsymbol{x}) = 0 \quad (\boldsymbol{x} \in \Gamma_0), \tag{40}$$

where the scaling function is constant: $\hat{\boldsymbol{\alpha}}(\boldsymbol{x}) = \alpha$ with $|\alpha| = 1$. This problem is ill-posed in the sense that it admits no non-null solutions in $H^{-1/2}(\Gamma)$. However it exhibits an essential spectrum given by (33) and associated with the strongly-oscillating singularities (13) illustrated in Figure 2a; thanks to the Dirichlet boundary condition on Γ_0, the two corners on Γ_0 do not contribute to the essential spectrum. This problem is well-suited to verify whether a discretization of $K_\alpha^\star$ is able to capture the deformation of the essential spectrum as $\arg(\alpha)$ is changed.

A discretization of (40) with the Nyström method described in Section 5.1 leads to a 2×2 block generalized eigenvalue problem on $(\sigma^h_{\alpha|\Gamma}, \sigma^h_{\alpha|\Gamma_0})$ that we reduce to an eigenvalue problem on $\sigma^h_{\alpha|\Gamma}$ using a Schur complement. We use an unstructured second-order graded mesh illustrated in Figure 11a; the grading is obtained by linearly interpolating the mesh size between $h_c \ll h$ and h:

$$h(r) = \left(1 - \frac{r}{R}\right)h_c + \frac{r}{R}h \quad (r \in (0, R]). \tag{41}$$

Figure 11b compares the computed eigenvalues to the exact essential spectrum for two values of the scaling parameter α. This shows qualitatively that the computed eigenvalues approximate the essential spectrum, although this is difficult to quantify due to the nature of the essential spectrum.

Figure 12 compares the Nyström results with those obtained with a $\mathcal{P}^2$-Lagrange isoparametric FEM for (24a) on Ω with a Dirichlet boundary condition on Γ_0. It illustrates that the FEM struggles to capture the essential spectrum for large values of $\arg(\alpha)$, although the agreement for small $\arg(\alpha)$ is satisfactory. Similarly to the ellipse case, this leads us to the conclusion that the Nyström method is more accurate on the same mesh.

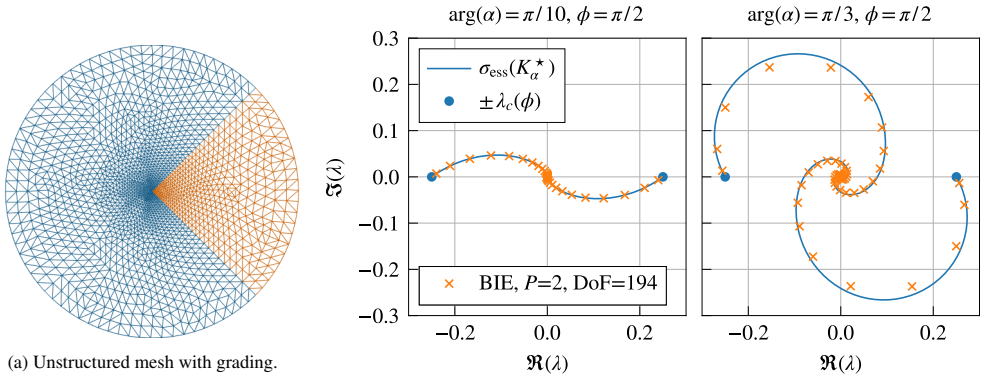

(a) Unstructured mesh with grading.

(b) Computed eigenvalues and exact spectrum (33) for various values of $\arg(\alpha)$.

Figure 11: Eigenvalue problem (40) with $R = 1$.

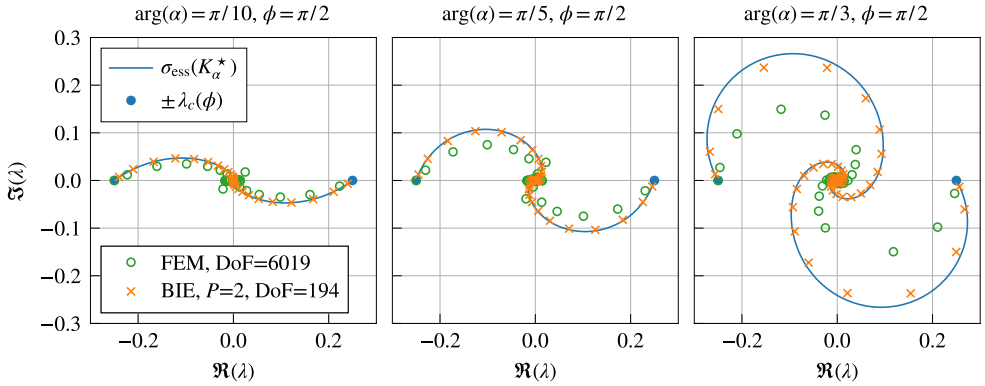

Figure 12: Eigenvalue problem (40) with $R = 1$. Comparison between Nyström and finite element.

5.4. Ellipse perturbed by corner

In this section, we consider two piecewise-smooth curves that exhibit complex resonances or embedded eigenvalues. Our first curve is an ellipse of semi-axes (a, b) perturbed by a straight

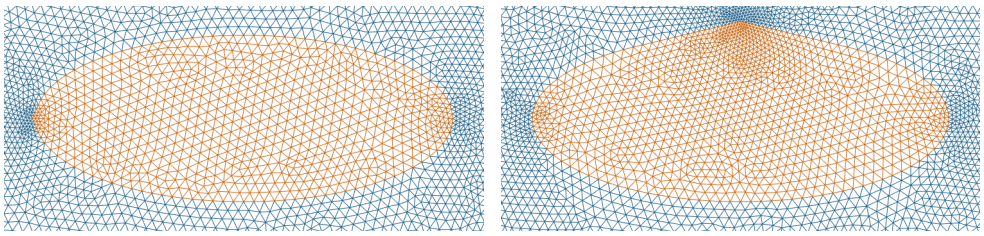

(a) Corner on major axis (42,43,44). (b) Corner on minor axis (45,46,47).

Figure 13: Mesh for an ellipse perturbed by a corner on its major or minor axis.

corner of angle ϕ on its major axis:

$$\begin{aligned}\Gamma = &\left\{(x,y) \,\middle|\, (x/a)^2 + (y/b)^2 = 1,\ x_m < x < a\right\} \\ &\cup \left\{ t\boldsymbol{x_c} + (1-t)\boldsymbol{x}_m^{\rho} \,\middle|\, t \in (0,1),\ \rho \in \{-,+\}\right\},\end{aligned} \tag{42}$$

where $\boldsymbol{x_c} = (x_c, 0)$ is the corner point and $\boldsymbol{x}_m^{\pm} = (x_m, \pm y_m)$ are the two junction points. We choose the parameters (x_c, x_m, y_m) so that Γ is C^1 at the two junction points $\boldsymbol{x_m^{\pm}}$:

$$(x_m/a)^2 + (y_m/b)^2 = 1,\ x_m/a = \frac{-\tan(\phi/2)}{\sqrt{(b/a)^2 + [\tan(\phi/2)]^2}},\ x_c - x_m = -y_m/\tan(\phi/2), \tag{43}$$

as illustrated in Figure 13a for

$$(a, b, \phi) = (2.5, 1, 0.75\pi), \tag{44}$$

which are the values we consider from now on. Γ satisfies Assumption 1 with "C^2" substituted by "$C^{1,1}$", which does not substantially change the theory. Most importantly for our purposes, for a given scaling parameter α, the essential spectrum is given by (33) and eigenvalues accumulate at 0. Our motivation for enforcing a C^1 junction with (43) is to prevent the two junction points $\boldsymbol{x_m^{\pm}}$ from contributing to the essential spectrum, thus enabling to isolate the effect of a single corner.

Before discussing the numerical results, we need to motivate our definition of Γ. The fact that "ellipse with corners" can exhibit embedded eigenvalues has first been reported in [1] and further analyzed in [2] where it is shown how one can construct piecewise-smooth curves that exhibit embedded eigenvalues. Let us apply the result of [2] to our boundary (42,43,44). We know that the ellipse has eigenvalues given by (39). When we modify the ellipse by adding a corner of angle $\phi \simeq \pi$, this is a small perturbation so that the perturbed eigenvalues will not move too much:

$$\lambda_j \simeq \lambda_j^{\mathrm{el}}.$$

However, the corner induces an essential spectrum $[-\lambda_c(\phi), \lambda_c(\phi)]$, which covers infinitely many ellipse eigenvalues. Let $\lambda_j^{\mathrm{el}} \in (-\lambda_c(\phi), \lambda_c(\phi))$ be a covered eigenvalue. The analysis in [2] shows that one can predict how this covered eigenvalue will be perturbed by studying the parity of the eigenfunction u_j^{el} with respect to the corner axis: if u_j^{el} has a parity opposite to that of the corner singularity (13), then there is no coupling and λ_j^{el} is perturbed into an embedded eigenvalue; otherwise λ_j^{el} is perturbed into a complex resonance.

When $\phi \in (0, \pi)$, the corner singularities are odd when $\lambda \in (0, \lambda_c(\phi))$ and even when $\lambda \in (-\lambda_c(\phi), 0)$. An investigation of the ellipse eigenfunctions, illustrated in Figure 8, shows that

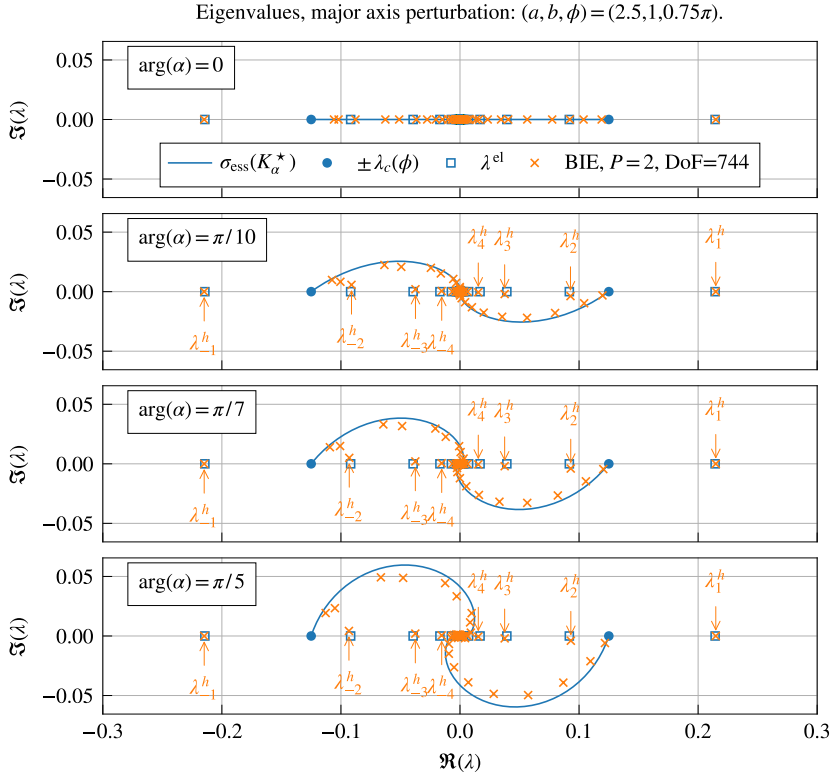

Figure 14: Ellipse perturbed by a corner on its major axis. Influence of $\arg(\alpha)$ on the eigenvalues computed using (38).

when λ_j^{el} is positive (resp. negative), the eigenfunction u_j^{el} is odd (resp. even) with respect to the major axis. Hence, we deduce that any eigenvalue satisfying $\lambda_j^{\mathrm{el}} \in [-\lambda_c(\phi), \lambda_c(\phi)]$ is perturbed into a complex resonance. In particular, there are no embedded eigenvalues.

Figure 14 plots the eigenvalues computed using the Nyström method for increasing values of $\arg(\alpha)$. For $\alpha = 1$, i.e. without complex scaling, only eigenvalues outside of the essential spectrum can be computed, the essential spectrum giving a cluster of eigenvalues. As $|\arg(\alpha)|$ is increased, the essential spectrum deforms and uncovers isolated eigenvalues, eight of them being highlighted in the plot and numbered such that $\lambda_j^h \simeq \lambda_j^{\mathrm{el}}$. Since the spectrum is invariant by $\lambda \mapsto -\lambda$ we numerically have $\lambda_i^h \simeq -\lambda_i^h$. The largest eigenvalue

$$\lambda_1^h \simeq 2.1 \times 10^{-1} - 3.6 \times 10^{-8} i$$

is an isolated eigenvalue of $K^\star$, which can be computed without complex scaling. The next three eigenvalues have significantly larger imaginary parts

$$\lambda_2^h \simeq 9.3 \times 10^{-2} - 4.0 \times 10^{-3} i,\ \lambda_3^h \simeq 3.8 \times 10^{-2} - 2.0 \times 10^{-3} i,\ \lambda_4^h \simeq 1.5 \times 10^{-2} - 5.2 \times 10^{-4} i,$$

from which we deduce that they are complex resonances. As $\lambda^h \to 0$, the imaginary parts of complex resonances tend to 0.

The associated complex-scaled eigenfunctions $u_{\alpha,j}^h = \mathcal{S}_\alpha^h \sigma_j^h$, which have a corner expansion of the form (28), are shown in Figure 15. All the eigenfunctions tend to zero in the complex

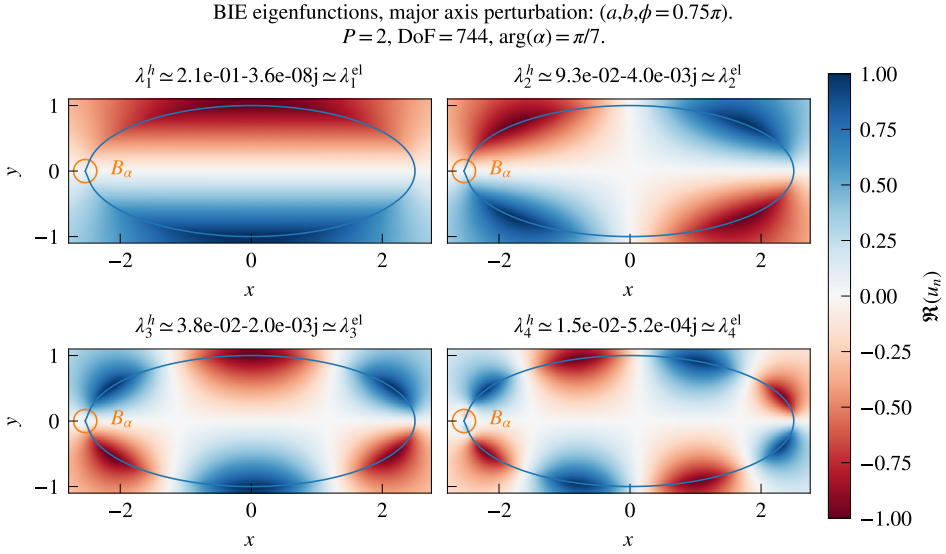

Figure 15: Ellipse perturbed by a corner on its major axis. Eigenfunctions.

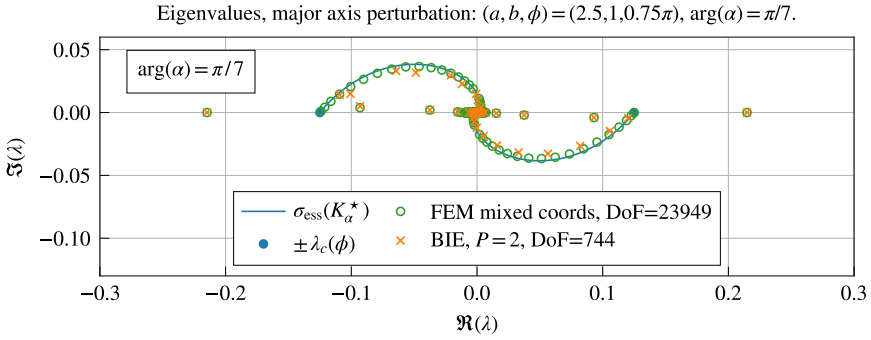

Figure 16: Ellipse perturbed by a corner on its major axis. Comparison with the FEM from [11].

scaling region B_α, which indicates that the complex scaling has tamed the exponentially growing singularity of the complex resonance functions ($j \in \{2,3,4\}$) while preserving the asymptotic behavior of the eigenfunction ($j=1$). At the entrance of the scaling region, a small oscillation can be seen for $u^h_{\alpha,4}$.

Figure 16 compares the spectrum obtained with the Nyström method with the one obtained using the FEM from [11], which discretizes (24a) in Euler coordinates around the corner and in Cartesian coordinates elsewhere; a Dirichlet-to-Neumann condition is enforced on a circular boundary to account for the decay condition (24b). Thanks to this mix of coordinate systems, this FEM is able to capture the essential spectrum with a high accuracy. The plot shows a satisfactory agreement on the complex resonances, which are the quantities of interest herein.

Our second obstacle is designed to obtain embedded eigenvalues. We consider the same

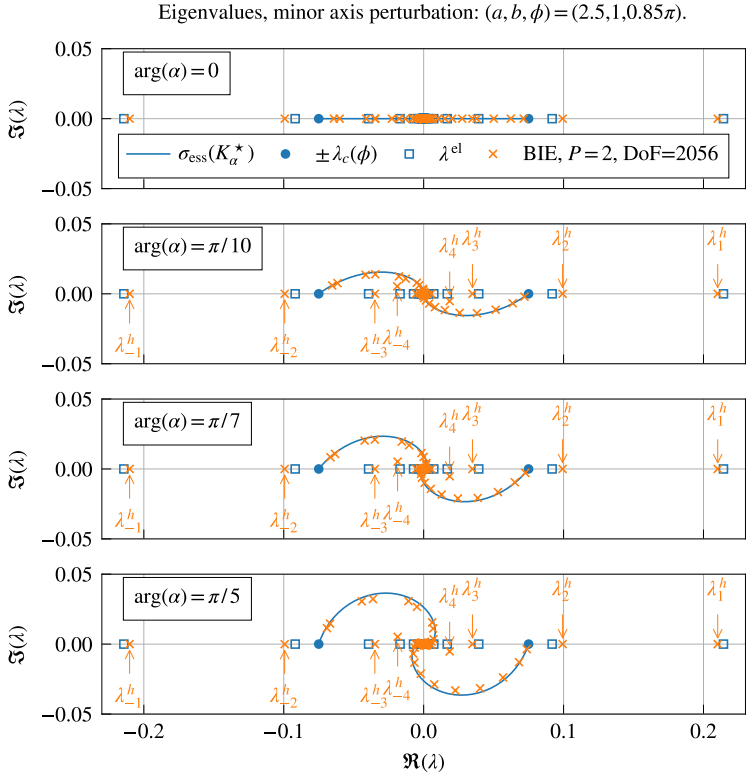

Figure 17: Ellipse perturbed by a corner on its minor axis. Influence of $\arg(\alpha)$ on eigenvalues computed using (38).

ellipse as above, but we add a corner of angle $\phi \in (0,\pi)$ on its minor axis instead:

$$\begin{aligned}\Gamma = &\left\{(x,y)\;\middle|\;(x/a)^2+(y/b)^2=1,\;-b<y<y_m\right\}\\ &\cup\left\{t\boldsymbol{x_c}+(1-t)\boldsymbol{x}_m^\rho\;\middle|\;t\in(0,1),\;\rho\in\{-,+\}\right\},\end{aligned} \tag{45}$$

where we enforce a C^1 junction using

$$(x_m/a)^2+(y_m/b)^2=1,\;\; x_m/a=\frac{1}{\sqrt{1+(b/a)^2\tan^2(\phi/2)}},\;\; y_c-y_m=x_m/\tan(\phi/2). \tag{46}$$

We focus on the case

$$(a,b,\phi)=(2.5,1,0.85\pi), \tag{47}$$

illustrated in Figure 13b. This corner perturbation is arguably not as "small" as the previous one, but the perturbation mechanism from [2] turns out to be still effective to understand its effect. Since ellipse eigenfunctions are alternatively odd and even with respect to $\{x=0\}$, ellipse eigenvalues will be alternatively perturbed into complex resonances and embedded eigenvalues.

Figure 17 plots the spectrum obtained with the Nyström method and highlights the largest isolated eigenvalues, the corresponding eigenfunctions being plotted in Figure 18. The eigenvalues λ_1^h and λ_2^h are isolated eigenvalues of $K^\star$, with imaginary parts around 10^{-7}. The eigenvalue

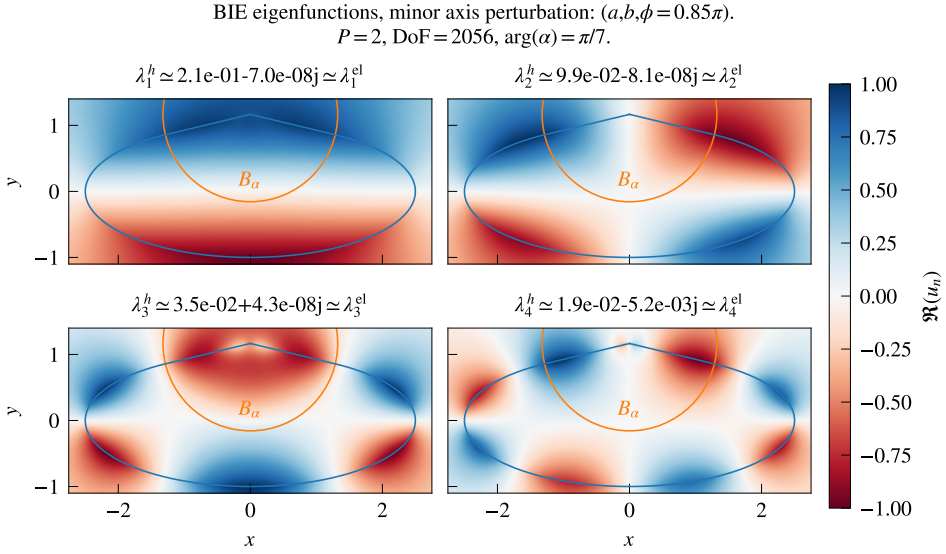

Figure 18: Ellipse perturbed by a corner on its minor axis. Eigenfunctions.

λ_3^h has an imaginary part with the same order of magnitude as λ_1^h and λ_2^h, which indicates that it is an embedded eigenvalue of $K^\star$; the associated eigenfunction is even with respect to the corner axis and thus does not couple with the odd corner singularity. Finally, since $|\Im(\lambda_4^h)|$ is four orders of magnitude larger than $|\Im(\lambda_1^h)|$, we deduce that it is a complex resonance, associated as expected with an odd eigenfunction. Inside the scaling region, we can see some oscillations of $u_{\alpha,4}$, which are attenuated before they reach the corner.

Let us now investigate the convergence of the computed eigenvalues and complex resonances. Since we use $P = 2$ with a second-order mesh, as for the ellipse validation case presented in Section 5.2, we can expect at most a $O(h^3)$ convergence rate. Given that we do not know the exact solutions, we estimate the error using

$$\max_{1\leq j\leq J} \left|\lambda_j^h - \lambda_j^{\text{ref}}\right| \tag{48}$$

where the reference values are the eigenvalues computed on a finer mesh. For this to be computationally tractable, we compute only a subset of the solutions of (38) using an implicitly restarted Arnoldi method through scipy [55].

Figure 19 plots the estimated relative errors for increasing values of $\arg(\alpha)$ using the grading (41) with $h_c = h^4$; the distance δ_d is set to the h-independent value $\delta_d = R/2$ where R is the radius of the scaling region B_α. For each eigenvalue, a convergence rate is estimated using a least squares fit on all the data points. The leftmost plot shows the convergence rate of the isolated eigenvalues $\lambda_{1,2}^h$ without complex scaling, which is lower than the one obtained for the ellipse. With complex scaling, the convergence rate of $\lambda_{1,2}^h$ remains around $O(h^2)$.

The convergence rate on the embedded eigenvalue λ_3^h is largest for $\arg(\alpha) = \pi/7$ while the estimated error is smaller for $\arg(\alpha) = \pi/10$. The complex resonance λ_4^h converges slowly for $\arg(\alpha) = \pi/10$, a value for which it is barely uncovered as shown in Figure 17. As $\arg(\alpha)$ is increased, both the convergence rate and error levels of λ_4^h improves, reaching at least a three-

digit accuracy on the finest mesh.

In summary, Figure 19 illustrates that there is no "one-size-fits-all", i.e. a value of $\arg(\alpha)$ that delivers an optimal convergence rate for all eigenvalues and complex resonances. Nonetheless, by choosing $\arg(\alpha) = \pi/7$ we are able to achieve at least a $O(h^2)$ rate for the four values considered.

The convergence rates shown in Figure 19 are both non-optimal and sensitive to the mesh grading at the corner, similarly to what happens for elliptic problems. In order to illustrate this, we now consider an *isogeometric* discretization of (45,46,47), i.e. we take $\Gamma^h = \Gamma$ with each map φ_n^h being defined from the analytical expression of Γ.

For the case $\arg(\alpha) = \pi/7$, the left plot of Figure 20 shows the estimated errors obtained without mesh grading. The eigenvalue λ_1^h converges linearly while the other three converge sub-linearly. This low convergence rate can be justified using the corner expansion (28), which is satisfied by the eigenfunctions. Near the corner, the density $\sigma = -[\![\partial_\nu u]\!]_\Gamma$ behaves like $r^{i\eta}$ with η close to the real axis. By solving the corner dispersion relations

$$g^{\mathfrak{e}}(\alpha\eta, \lambda_j^h) = 0, \;\; g^{\mathfrak{o}}(\alpha\eta, \lambda_j^h) = 0,$$

where $g^{\mathfrak{e}}$ and $g^{\mathfrak{o}}$ are given by (12), we deduce that for each of the four eigenfunctions the radial exponent that drives the regularity is

$$\eta_1^h \simeq -0.9 - 1.1i, \;\; \eta_2^h \simeq -0.18 - 0.37i, \;\; \eta_3^h \simeq -1.5 - 0.77i, \;\; \eta_4^h \simeq 1 - 0.34i.$$

From these values we deduce that $r \mapsto r^{i\eta_k^h}$ is C^1 at $r = 0$ only for $k = 1$, which explains the slow convergence observed without grading. The right plot of Figure 20 shows the errors obtained with the corner grading $\mu : [0,1] \to [0,1]$ defined in [49, (2.2)] with the parameter "$p = 4$", which satisfies $\mu^{(m)}(0) = 0$ for $m \in \{1,2,3\}$: this property increases the regularity of the integrand at $r = 0$ and leads to improved convergence rates, delivering a convergence close to third-order. However, this grading is not tailored to the strongly-oscillating singularities (13): the waveguide viewpoint recalled in Section 3.1, which takes place in Euler coordinates $(z = \ln r, \theta)$, suggests that a better grading would be exponential, for instance $\mu(r) = \exp(1 - 1/r)$. Unfortunately, the implementation of such a grading in double precision arithmetic is delicate due to loss of significant digits.

5.5. Delta geometry

Let $\phi \in (\pi, 2\pi)$. We consider the "delta" geometry, adapted from [49]:

$$\Gamma = \left\{ \left(-\frac{2\sin(3t/2)}{3\tan(\phi/2)}, -\sin(t) \right) \,|\, t \in (0, 2\pi) \right\}, \tag{49}$$

which defines the boundary of a non-convex domain Ω having a reentrant corner of angle ϕ at $\boldsymbol{x_c} = (0,0)$. This domain does not satisfy Assumption 1 since its corner is not straight. However, the corner is "almost" straight in the sense that

$$|\theta(r)| - (\pi - \phi/2) \underset{r\to 0}{=} O(r^2),$$

where (r, θ) are the polar coordinates centered at $\boldsymbol{x_c}$, so that we can expect that the complex scaling introduced in this work can still be applied. To verify this, we now consider an isogeometric

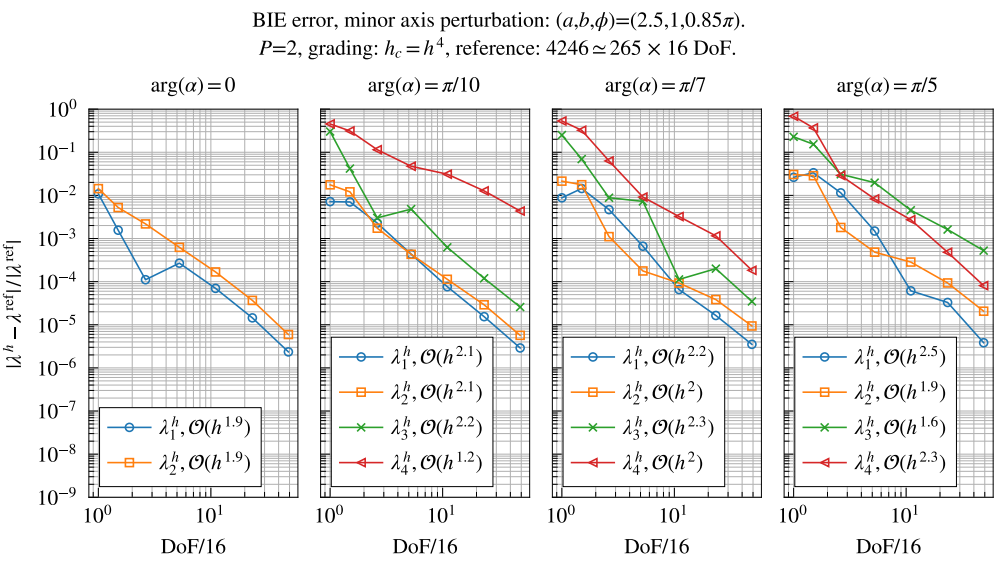

Figure 19: Ellipse perturbed by a corner on its minor axis (45,46,47). Estimated error (48) with Nyström method.

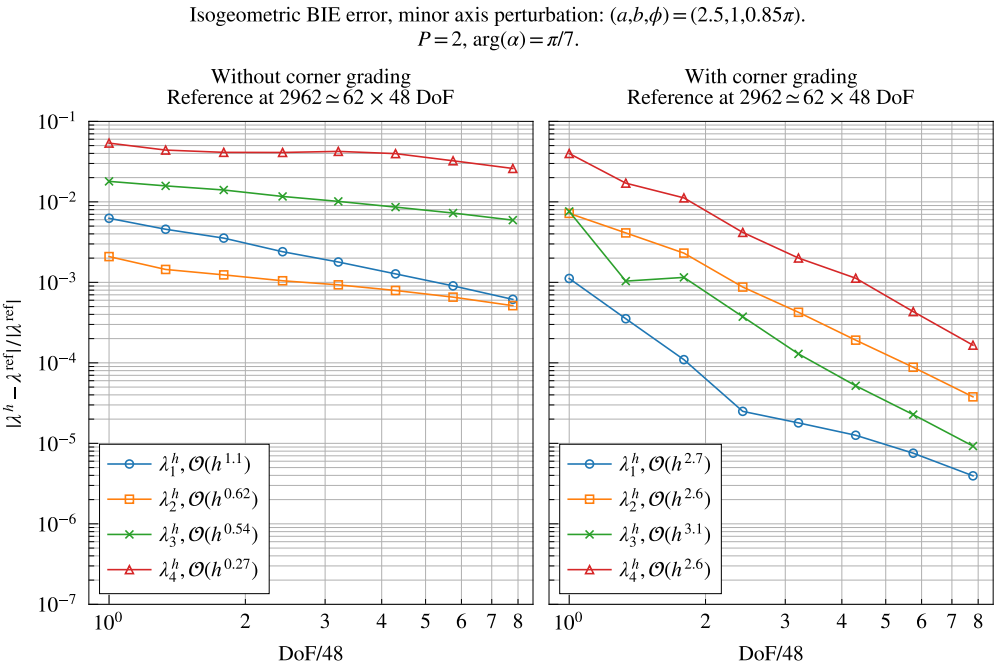

Figure 20: Ellipse perturbed by a corner on its major axis. Estimated error (48) with a Nyström method using an isogeometric discretization with different mesh gradings at the corner.

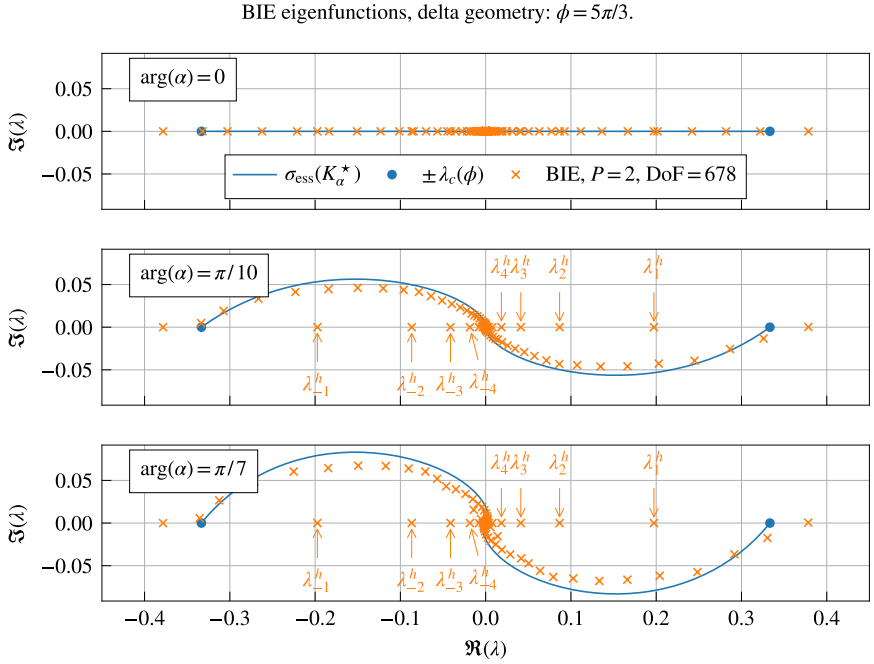

Figure 21: Delta geometry (49). Eigenvalues obtained with (38).

discretization of Γ with angle $\phi = 5\pi/3$. At the corner, we use the grading defined in [49, (2.2)] with parameter "$p = 3$". To reduce spectral pollution, we increase P_s to $P_s = 8$ for this case.

Figure 21 plots the eigenvalues obtained by solving (38) with a scaling region of radius $R_\alpha = 0.4$, slightly adjusted to ensure mesh conformity. It illustrates that the complex scaling is able to deform the essential spectrum; eight of the uncovered embedded eigenvalues are highlighted. The eigenfunctions associated with the first three embedded eigenvalues are shown in Figure 22. By contrast with the results of Section 5.4, these eigenfunctions are odd with respect to the corner axis. This follows from the fact that when $\phi \in (\pi, 2\pi)$, the strongly-oscillating corner singularities associated with $\lambda \in (0, \lambda_c(\phi))$ are even. Hence, for this boundary, positive embedded eigenvalues are associated odd eigenfunctions while negative embedded eigenvalues are associated with even eigenfunctions.

Overall, this example illustrates that the complex-scaled NP operator derived in this work can be applied to domains with non-straight corners, at least as long as the corner does not exhibit a strong curvature.

6. Conclusion and outlook

In this work we focused on the computation of complex resonances and embedded eigenvalues of the Neumann-Poincaré operator (1) on domains with straight corners (Assumption 1) using a BIE. Our strategy was to adapt the corner complex scaling technique [10], originally developed for (5), to (4). Based on previous works involving complex scaling in BIEs [12, 13], this adaptation is simple in principle and can be broken down as follows:

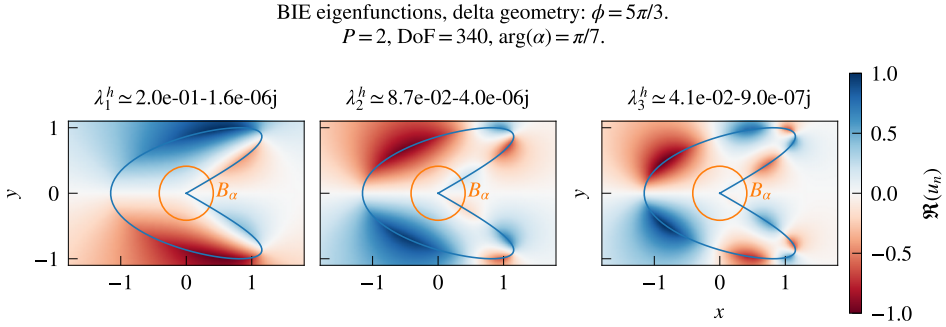

Figure 22: Delta geometry (49). Eigenfunctions obtained with (38).

1. formulate the complex scaling as a path $\Gamma_\alpha : \mathbb{R}^2 \to \mathbb{C}^2$,
2. define the complex-scaled Green's function as "$G_\alpha(\boldsymbol{x}, \boldsymbol{y}) = G(\Gamma_\alpha(\boldsymbol{x}), \Gamma_\alpha(\boldsymbol{y}))$",
3. define the complex-scaled NP operator (31).

However, in carrying out this program we encountered two hurdles. Firstly, corner complex scaling is defined in [10] as a linear scaling in Euler coordinates (z, θ); mapping back to Cartesian coordinates leads to the unwieldy nonlinear expression (20). Secondly, the formula for G_α suggested above turns out to have discontinuities close to the corner due to $\Gamma_\alpha(\boldsymbol{x}) - \Gamma_\alpha(\boldsymbol{y})$ crossing the branch cut of ln. The location of these discontinuities implies that they are not a major computational issue, however for completeness we proposed the corrected expression (34).

Eventually, the scaled NP operator simplifies to (35) and a Nyström method leads to the dense linear non-hermitian eigenvalue problem (38). Solving this problem using standard packages enabled us to compute both complex resonances and embedded eigenvalues, see Figures 14 and 17, with a convergence rate between second and third order.

Let us suggest directions for future work. Firstly, this scaling can be directly applied to the Helmholtz scattering problem on domains with corners, which should lead to a convergent scheme even when the source term excites the strongly-oscillating corner singularities. However, using this scaling for the Helmholtz eigenvalue problem is much more challenging due to the nonlinearity in the spectral parameter.

Secondly, improving the convergence rates shown in Figures 19 and 20 could lead to interesting developments. As suggested at the end of Section 5.4, implementing a grading tailored to the expression of strongly-oscillating singularities could be beneficial. Moreover, the dependency of the convergence rates on both $\arg(\alpha)$ and λ suggests that there might be room for improvement in the expression of the scaling function $\hat{\alpha}$.

Code Availability Statement

The code used to generate the findings of this study is openly available on Github at `https://doi.org/10.5281/zenodo.16309756`.

References

[1] J. Helsing, H. Kang, M. Lim, Classification of spectra of the Neumann–Poincaré operator on planar domains with corners by resonance, Annales de l'Institut Henri Poincare (C) Non Linear Analysis 34 (2017) 991–1011. doi:10.1016/j.anihpc.2016.07.004.

[2] W. Li, S. P. Shipman, Embedded eigenvalues for the Neumann-Poincaré operator, Journal of Integral Equations and Applications 31 (2019) 505–534. doi:10.1216/JIE-2019-31-4-505.
[3] D. Colton, R. Kress, Integral Equation Methods in Scattering Theory, 1 ed., Wiley, New York, 1983.
[4] D. Khavinson, M. Putinar, H. S. Shapiro, Poincaré's variational problem in potential theory, Archive for Rational Mechanics and Analysis 185 (2007) 143–184. doi:10.1007/s00205-006-0045-1.
[5] K.-M. Perfekt, M. Putinar, The essential spectrum of the Neumann–Poincaré operator on a domain with corners, Archive for Rational Mechanics and Analysis 223 (2017) 1019–1033. doi:10.1007/s00205-016-1051-6.
[6] M. Costabel, Boundary integral operators on Lipschitz domains: Elementary results, SIAM Journal on Mathematical Analysis 19 (1988) 613–626. doi:10.1137/0519043.
[7] D. Mitrea, The method of layer potentials for non-smooth domains with arbitrary topology, Integral Equations and Operator Theory 29 (1997) 320–338. doi:10.1007/BF01320705.
[8] W. McLean, Strongly Elliptic Systems and Boundary Integral Equations, Cambridge University Press, Cambridge, 2000.
[9] S. Dyatlov, M. Zworski, Mathematical Theory of Scattering Resonances, American Mathematical Society, Providence, Rhode Island, 2019.
[10] A.-S. Bonnet-Ben Dhia, C. Carvalho, L. Chesnel, P. Ciarlet, On the use of perfectly matched layers at corners for scattering problems with sign-changing coefficients, Journal of Computational Physics 322 (2016) 224–247. doi:10.1016/j.jcp.2016.06.037.
[11] A.-S. Bonnet-Ben Dhia, C. Hazard, F. Monteghetti, Complex-scaling method for the complex plasmonic resonances of planar subwavelength particles with corners, Journal of Computational Physics 440 (2021) 110433. doi:10.1016/j.jcp.2021.110433.
[12] W. Lu, Y. Y. Lu, J. Qian, Perfectly Matched Layer Boundary Integral Equation Method for Wave Scattering in a Layered Medium, SIAM Journal on Applied Mathematics (2018). doi:10.1137/17M1112510.
[13] A.-S. B.-B. Dhia, L. M. Faria, C. Pérez-Arancibia, A Complex-Scaled Boundary Integral Equation for Time-Harmonic Water Waves, SIAM J. Appl. Math. (2024). doi:10.1137/23M1607866.
[14] A.-S. Bonnet-Ben Dhia, L. Chesnel, X. Claeys, Radiation condition for a non-smooth interface between a dielectric and a metamaterial, Mathematical Models and Methods in Applied Sciences 23 (2013) 1629–1662. doi:10.1142/S0218202513500188.
[15] S. Maier, Plasmonics fundamentals and applications, Springer, New York, 2007.
[16] D. Sarid, W. Challener, Modern Introduction to Surface Plasmons, Cambridge University Press, Cambridge, 2010.
[17] I. D. Mayergoyz, Plasmon Resonances in Nanoparticles, 1 ed., World Scientific, New Jersey, 2013.
[18] K. Ando, H. Kang, Y. Miyanishi, M. Putinar, Spectral analysis of Neumann-Poincare operator, Romanian Journal of Pure and Applied Mathematics (2021).
[19] H. Ammari, B. Fitzpatrick, H. Kang, M. Ruiz, S. Yu, H. Zhang, Mathematical and computational methods in photonics and phononics, volume 235, American Mathematical Society, Providence, Rhode Island, 2018.
[20] K.-M. Perfekt, M. Putinar, Spectral bounds for the Neumann-Poincaré operator on planar domains with corners, Journal d'Analyse Mathématique 124 (2014) 39–57. doi:10.1007/s11854-014-0026-5.
[21] L. Escauriaza, E. B. Fabes, G. Verchota, On a regularity theorem for weak solutions to transmission problems with internal Lipschitz boundaries, Proceedings of the American Mathematical Society 115 (1992) 1069–1076. doi:10.1090/S0002-9939-1992-1092919-1.
[22] T. Chang, K. Lee, Spectral properties of the layer potentials on Lipschitz domains, Illinois Journal of Mathematics 52 (2008) 463 – 472. doi:10.1215/ijm/1248355344.
[23] G. Verchota, Layer potentials and regularity for the Dirichlet problem for Laplace's equation in Lipschitz domains, Journal of Functional Analysis 59 (1984) 572–611. doi:10.1016/0022-1236(84)90066-1.
[24] J. F. Ahner, Some spectral properties of an integral operator in potential theory, Proceedings of the Edinburgh Mathematical Society 29 (1986) 405–411. doi:10.1017/S0013091500017843.
[25] D. Grieser, The plasmonic eigenvalue problem, Reviews in Mathematical Physics 26 (2014) 1450005. doi:10.1142/S0129055X14500056.
[26] O. Schnitzer, Geometric quantization of localized surface plasmons, IMA Journal of Applied Mathematics 84 (2019) 813–832. doi:10.1093/imamat/hxz016.
[27] Blåsten, Emilia, Li, Hongjie, Liu, Hongyu, Wang, Yuliang, Localization and geometrization in plasmon resonances and geometric structures of Neumann-Poincaré eigenfunctions, ESAIM: M2AN 54 (2020) 957–976. doi:10.1051/m2an/2019091.
[28] E. Bonnetier, H. Zhang, Characterization of the essential spectrum of the Neumann–Poincaré operator in 2D domains with corner via Weyl sequences, Revista Matemática Iberoamericana 35 (2019) 925–948. doi:10.4171/rmi/1075.
[29] K.-M. Perfekt, Plasmonic eigenvalue problem for corners: Limiting absorption principle and absolute continuity in the essential spectrum, Journal de Mathématiques Pures et Appliquées 145 (2021) 130–162. doi:10.1016/j.matpur.2020.07.001.

[30] I. D. Mayergoyz, D. R. Fredkin, Z. Zhang, Electrostatic (plasmon) resonances in nanoparticles, Physical Review B 72 (2005) 155412. doi:10.1103/PhysRevB.72.155412.
[31] G. Demésy, A. Nicolet, B. Gralak, C. Geuzaine, C. Campos, J. E. Roman, Non-linear eigenvalue problems with GetDP and SLEPc: Eigenmode computations of frequency-dispersive photonic open structures, Computer Physics Communications 257 (2020) 107509. doi:10.1016/j.cpc.2020.107509.
[32] M. D. Truong, A. Nicolet, G. Demésy, F. Zolla, Continuous family of exact dispersive quasi-normal modal (DQNM) expansions for dispersive photonic structures, Optics Express 28 (2020) 29016–29032. doi:10.1364/OE.401742.
[33] A.-S. Bonnet-Ben Dhia, C. Carvalho, P. Ciarlet, Mesh requirements for the finite element approximation of problems with sign-changing coefficients, Numerische Mathematik 138 (2018) 801–838. doi:10.1007/s00211-017-0923-5.
[34] A. Abdulle, M. E. Huber, S. Lemaire, An optimization-based numerical method for diffusion problems with sign-changing coefficients, C. R. Math. 355 (2017) 472–478. doi:10.1016/j.crma.2017.02.010.
[35] P. Ciarlet, D. Lassounon, M. Rihani, An Optimal Control-Based Numerical Method for Scalar Transmission Problems with Sign-Changing Coefficients, SIAM Journal on Numerical Analysis (2023). doi:10.1137/22M1495998.
[36] J. Helsing, Solving Integral Equations on Piecewise Smooth Boundaries Using the RCIP Method: A Tutorial, Abstract and Applied Analysis 2013 (2013). doi:10.1155/2013/938167.
[37] J. Helsing, A. Karlsson, On a Helmholtz transmission problem in planar domains with corners, Journal of Computational Physics 371 (2018) 315–332. doi:10.1016/j.jcp.2018.05.044.
[38] F. Ouyang, M. Isaacson, Surface plasmon excitation of objects with arbitrary shape and dielectric constant, Philosophical Magazine B 60 (1989) 481–492. doi:10.1080/13642818908205921.
[39] H. Kang, J. Seo, Recent progress in the inverse conductivity problem with single measurement, in: G. Nakamura, J. Seo, M. Yamamoto (Eds.), Inverse problems and related topics, Chapman & Hall/CRC, Boca Raton, 2000, pp. 69–80.
[40] J. Helsing, K.-M. Perfekt, On the polarizability and capacitance of the cube, Applied and Computational Harmonic Analysis 34 (2013) 445–468. doi:10.1016/j.acha.2012.07.006.
[41] V. A. Kondrat'ev, O. A. Oleinik, Boundary-value problems for partial differential equations in non-smooth domains, Russian Mathematical Surveys 38 (1983) 1–86. doi:10.1070/rm1983v038n02abeh003470.
[42] P. Grisvard, Elliptic Problems in Nonsmooth Domains, Pitman Publishing, London, 1985.
[43] M. Dauge, Elliptic boundary value problems on corner domains, Springer-Verlag, Berlin, 1988.
[44] M. Dauge, B. Texier, Problèmes de transmission non coercifs dans des polygones, 1997. Hal-00562329.
[45] M. Costabel, M. Dauge, Singularities of electromagnetic fields in polyhedral domains, Archive for Rational Mechanics and Analysis 151 (2000) 221–276. doi:10.1007/s002050050197.
[46] J. Aguilar, J. M. Combes, A class of analytic perturbations for one-body Schrödinger hamiltonians, Communications in Mathematical Physics 22 (1971) 269–279. doi:10.1007/BF01877510.
[47] E. Balslev, J. M. Combes, Spectral properties of many-body Schrödinger operators with dilatation-analytic interactions, Communications in Mathematical Physics 22 (1971) 280–294. doi:10.1007/BF01877511.
[48] K. Atkinson, Numerical Analysis, 3 ed., Springer, Dordrecht, 2009.
[49] R. Kress, A Nyström method for boundary integral equations in domains with corners, Numer. Math. 58 (1990) 145–161. doi:10.1007/BF01385616.
[50] C. Geuzaine, J.-F. Remacle, Gmsh: A 3-D finite element mesh generator with built-in pre- and post-processing facilities, Int. J. Numer. Methods Eng. 79 (2009) 1309–1331. doi:10.1002/nme.2579.
[51] K. E. Atkinson, The Numerical Solution of Integral Equations of the Second Kind, Cambridge University Press, Cambridge, 1997.
[52] C. R. Harris, K. J. Millman, S. J. van der Walt, R. Gommers, P. Virtanen, D. Cournapeau, E. Wieser, J. Taylor, S. Berg, N. J. Smith, R. Kern, M. Picus, S. Hoyer, M. H. van Kerkwijk, M. Brett, A. Haldane, J. F. del Río, M. Wiebe, P. Peterson, P. Gérard-Marchant, K. Sheppard, T. Reddy, W. Weckesser, H. Abbasi, C. Gohlke, T. E. Oliphant, Array programming with NumPy, Nature 585 (2020) 357–362. doi:10.1038/s41586-020-2649-2.
[53] J. Bremer, A fast direct solver for the integral equations of scattering theory on planar curves with corners, Journal of Computational Physics 231 (2012) 1879–1899. doi:10.1016/j.jcp.2011.11.015.
[54] O. P. Bruno, E. Garza, A Chebyshev-based rectangular-polar integral solver for scattering by geometries described by non-overlapping patches, J. Comput. Phys. 421 (2020) 109740. doi:10.1016/j.jcp.2020.109740.
[55] P. Virtanen, R. Gommers, T. E. Oliphant, M. Haberland, T. Reddy, D. Cournapeau, E. Burovski, P. Peterson, W. Weckesser, J. Bright, S. J. van der Walt, M. Brett, J. Wilson, K. J. Millman, N. Mayorov, A. R. J. Nelson, E. Jones, R. Kern, E. Larson, C. J. Carey, İ. Polat, Y. Feng, E. W. Moore, J. VanderPlas, D. Laxalde, J. Perktold, R. Cimrman, I. Henriksen, E. A. Quintero, C. R. Harris, A. M. Archibald, A. H. Ribeiro, F. Pedregosa, P. van Mulbregt, SciPy 1.0 Contributors, SciPy 1.0: Fundamental Algorithms for Scientific Computing in Python, Nature Methods 17 (2020) 261–272. doi:10.1038/s41592-019-0686-2.

A. Boundary integral operators for strongly elliptic problems

In this section we gather standard results on BI operators associated with scalar strongly elliptic problems with smooth coefficients; we refer to [6, 8] for further background. Throughout this appendix, $\mathcal{P}$ denotes the second-order operator

$$\mathcal{P}u = -\nabla \cdot [A\nabla u],$$

where the coefficients satisfy $A \in L^\infty(\mathbb{R}^2; \mathbb{C}^{2\times 2}) \cap C^\infty(\mathbb{R}^2; \mathbb{C}^{2\times 2})$, $A^T = A$, and

$$\exists c_0, c_1 > 0 : \ \forall (\boldsymbol{x}, \xi) \in \mathbb{R}^2 \times \mathbb{R}^2, \ c_0|\xi|^2 \le \Re[A(\boldsymbol{x})\xi \cdot \xi] \le c_1|\xi|^2.$$

For any $\varphi \in C_c^\infty(\mathbb{R}^2)$, we define the conormal derivative $\partial_{A,\nu} u = [A\nabla u] \cdot \nu$, which through the first Green identity defines two one-sided trace operators $\partial_{A,\nu}^\pm : H^1_{\mathcal{P}}(\Omega^\pm) \to H^{-1/2}(\Gamma)$ where [6, Lem. 3.2]

$$H^1_{\mathcal{P}}(\Omega^\pm) = \{u \in H^1(\Omega^\pm) \,|\, \mathcal{P}u \in L^2(\Omega^\pm)\}. \tag{A.1}$$

Let $G(\boldsymbol{x}, \boldsymbol{y})$ be the solution of $\mathcal{P}G(\cdot, \boldsymbol{y}) = \delta(\cdot - \boldsymbol{y})$. Using G and $\partial_{A,\nu}$, we can define the single and double layer potentials

$$\mathcal{S}\sigma(\boldsymbol{x}) = \int_\Gamma G(\boldsymbol{x}, \boldsymbol{y})\sigma(\boldsymbol{y}) \,\mathrm{d}s(\boldsymbol{y}), \ \mathcal{K}\sigma(\boldsymbol{x}) = \int_\Gamma \partial_{A,\nu(\boldsymbol{y})} G(\boldsymbol{x}, \boldsymbol{y})\sigma(\boldsymbol{y}) \,\mathrm{d}s(\boldsymbol{y}) \quad (\boldsymbol{x} \in \mathbb{R}^2 \backslash \Gamma),$$

as well as the single and double layer operators

$$S\,\sigma(\boldsymbol{x}) = \int_\Gamma G(\boldsymbol{x}, \boldsymbol{y})\sigma(\boldsymbol{y}) \,\mathrm{d}s(\boldsymbol{y}), \ K\sigma(\boldsymbol{x}) = \mathrm{pv} \int_\Gamma \partial_{A,\nu(\boldsymbol{y})} G(\boldsymbol{x}, \boldsymbol{y})\sigma(\boldsymbol{y}) \,\mathrm{d}s(\boldsymbol{y}) \quad (\boldsymbol{x} \in \Gamma).$$

Now let $\Omega \subset \mathbb{R}^2$ be a bounded open set with a Lipschitz boundary Γ. The following standard properties hold.

Proposition 26 (Sobolev mapping properties)**.** *The layer potentials and BI operators satisfy*

$$\mathcal{S} : \ H^{-1/2}(\Gamma) \to H^1_{\mathrm{loc}}(\mathbb{R}^2), \ \mathcal{K} : \ H^{1/2}(\Gamma) \to L^2_{\mathrm{loc}}(\mathbb{R}^2),$$
$$S \in \mathcal{B}(H^{-1/2}(\Gamma), H^{1/2}(\Gamma)), \ K \in \mathcal{B}(H^{1/2}(\Gamma), H^{1/2}(\Gamma)).$$

Proof. See [6, Thm. 1]. □

Proposition 27 (Jump relations)**.** *The single layer potential satisfies the jump relations*

$$\forall \sigma \in H^{-1/2}(\Gamma), \ [\![\mathcal{S}\sigma]\!]_\Gamma = 0, \ \partial_{A,\nu}^\pm \mathcal{S}\sigma = K^\star\sigma \mp \frac{1}{2}\sigma.$$

Proof. See [6, Lem. 4.1]. □

Proposition 28 (Third Green identity)**.** *Let $u \in L^2(\mathbb{R}^2)$ with compact support. If $u_{|\Omega} \in H^1_{\mathcal{P}}(\Omega)$ and $u_{|\Omega^c} \in H^1_{\mathcal{P}}(\Omega^c)$, then for a.e. $\boldsymbol{x} \in \mathbb{R}^2$,*

$$u(\boldsymbol{x}) = \int_\Omega G(\boldsymbol{x}, \boldsymbol{y})Pu(\boldsymbol{y}) \,\mathrm{d}\boldsymbol{y} + \int_{\Omega^c} G(\boldsymbol{x}, \boldsymbol{y})Pu(\boldsymbol{y}) \,\mathrm{d}\boldsymbol{y} - \mathcal{S}[\![\partial_{A,\nu} u]\!]_\Gamma(\boldsymbol{x}) + \mathcal{K}[\![u]\!]_\Gamma(\boldsymbol{x}), \tag{A.2}$$

where the jumps are defined as (8).

Proof. See [8, Thm. 6.10] or [6, Lem. 3.4]. □

Lemma 29. *Let $\sigma \in H^{-1/2}(\Gamma)$ be a non-null solution of $K^\star\sigma = \lambda\sigma$ for some $\lambda \in \mathbb{R}$. The following equivalence holds: $\langle \sigma, 1\rangle_{-1/2,1/2} = 0 \Leftrightarrow \lambda \neq -1/2$.*

Proof. Testing $K^\star\sigma = \lambda\sigma$ against 1 leads to $\langle \sigma, K[1]\rangle_{-1/2,1/2} = \lambda \langle \sigma, 1\rangle_{-1/2,1/2}$, so that the claim follows from $K[1] = -1/2$. (Apply Proposition 28 to $u = \mathbb{1}_\Omega$, take the interior trace $\gamma_0^- : H^1(\Omega) \to H^{1/2}(\Gamma)$ to obtain $1 = -\gamma_0^-(\mathcal{K}[1])$, and use $\gamma_0^-\mathcal{K}\sigma = (K - I/2)\sigma$). □

Lemma 30. *Let $\sigma \in H^{-1/2}(\Gamma)$ such that $\langle \sigma, 1\rangle_{-1/2,1/2} = 0$. If $S\sigma = 0$, then $\sigma = 0$.*

Proof. Let $\sigma \in H^{-1/2}(\Gamma)$ such that $\langle \sigma, 1\rangle_{-1/2,1/2} = 0$ and $S\sigma = 0$ a.e. on Γ. Let $v = \mathcal{S}\sigma \in H^1_{\mathrm{loc}}(\mathbb{R}^2)$ be the associated single layer potential. The jump relations imply that the trace and conormal derivative of v satisfies $v_{|\Gamma} = 0$ and $\partial^-_{A,\nu} v = (K^\star + I/2)\,\sigma$. However, since $\mathcal{P}v = 0$ in Ω we deduce using the first Green's identity on Ω that v is constant. Hence $K^\star\sigma = -\sigma/2$ and we conclude using Lemma 29 that $\sigma = 0$. □

Using the above results we can prove the following equivalence.

Proposition 31. *Let $\lambda \in \mathbb{C}\backslash\{\pm 1/2\}$ and κ be given by (6). Let $R > 0$ be a radius such that $A(x) = I$ when $|x| > R$.*

(i) *If $\sigma \in H^{-1/2}(\Gamma)\backslash\{0\}$ solves $K^\star\sigma = \lambda\sigma$, then $u = \mathcal{S}\sigma \in \dot{H}^1(\mathbb{R}^2)$ is a non-null solution of*

$$\nabla \cdot [a(\boldsymbol{x}, \kappa)A(\boldsymbol{x})\nabla u(\boldsymbol{x})] = 0 \tag{A.3a}$$

$$u(\boldsymbol{x}) \underset{|\boldsymbol{x}|\to\infty}{=} O(|\boldsymbol{x}|^{-1}). \tag{A.3b}$$

(ii) *If $u \in \dot{H}^1(\mathbb{R}^2)$ is a non-null solution of (A.3), then $\sigma = -[\![\partial_{A,\nu} u]\!]_\Gamma \in H^{-1/2}(\Gamma)$ is a non-null solution of $K^\star\sigma = \lambda\sigma$.*

Proof. Let $\lambda \in \mathbb{C}\backslash\{\pm 1/2\}$ and κ be given by (6).

(i) Let $\sigma \in H^{-1/2}(\Gamma)$ be a non-null solution of $K^\star\sigma = \lambda\sigma$. Since $\lambda \neq -1/2$, we deduce from Lemma 29 that $\langle \sigma, 1\rangle_{-1/2,1/2} = 0$. Let us now check that $u = \mathcal{S}\sigma$ solves (A.3). By construction, $\mathcal{P}u = 0$ on $\Omega \cup \Omega^c$. The asymptotic identity

$$\mathcal{S}\sigma(\boldsymbol{x}) \underset{|\boldsymbol{x}|\to\infty}{=} \langle \sigma, 1\rangle_{-1/2,1/2} \times C \ln|\boldsymbol{x}| + O(|\boldsymbol{x}|^{-1}), \tag{A.4}$$

where C is some constant, implies that u satisfies the decay condition (A.3b). Since $u \in H^1_{\mathrm{loc}}(\mathbb{R}^2)$, it satisfies $[\![u]\!]_\Gamma = 0$; injecting the jump relations into $[\![a(\cdot,\kappa)\partial_{A,\nu}u]\!]_\Gamma = 0$ leads to

$$K^\star\sigma(\boldsymbol{x}) + \sigma(\boldsymbol{x})/2 = \kappa\left[K^\star\sigma(\boldsymbol{x}) - \sigma(\boldsymbol{x})/2\right] \quad (\boldsymbol{x} \in \Gamma),$$

which is $K^\star\sigma = \lambda\sigma$ since by assumption (6) holds. It remains to check that u is non-null. Lemma 30 implies that $u_{|\Gamma} \neq 0$ in $H^{1/2}(\Gamma)$, from which we deduce that $u \neq 0$ in $H^1(\Omega)$ from the uniqueness of the solution to the Dirichlet boundary value problem on Ω.

(ii) Let $u \in \dot{H}^1(\mathbb{R}^2)$ be a non-null solution of (A.3). Since $u \in H^1_{\mathrm{loc}}(\mathbb{R}^2)$, $[\![u]\!]_\Gamma = 0$ in $H^{1/2}(\Gamma)$. Let $\sigma = -[\![\partial_{A,\nu}u]\!]_\Gamma$ in $H^{-1/2}(\Gamma)$ and $v = \mathcal{S}\sigma$. Proposition 28 , combined with the behavior at infinity of u, implies that for any $\chi \in C^\infty_c(\mathbb{R}^n)$, $\chi(u - v) = 0$. The jump relations imply that σ solves $K^\star\sigma = \lambda\sigma$. Moreover, since $\lambda \neq -1/2$, we deduce from Lemma 29 that $\langle \sigma, 1\rangle_{-1/2,1/2} = 0$, so that (A.4) implies that v satisfies the decay condition (A.3b), so that $u = v$ a.e. in $\mathbb{R}^2$. Finally, $\sigma \neq 0$ since otherwise v, hence u would be null.

□

B. Derivation of the complex-scaled Green's function

This section gathers technical lemmas used in the derivation of the complex-scaled Green's function presented in Section 4.

B.1. Complex-scaled distances

This section focuses on the complex-scaled squared distance terms q_α and $\hat{q}_\alpha$, which are used as arguments of the principal branch of the logarithm in the definition of the complex-scaled Green's function. The objective of the results below is to verify that q_α and $\hat{q}_\alpha$ do not cross the real negative axis on their domains of definition.

Lemma 32. *Let $\Re(\alpha) > 0$. For any $(\boldsymbol{x}, \boldsymbol{y}) \in \mathbb{R}^4 \backslash B_\alpha^2$, we have*

1. $q_\alpha(\boldsymbol{x}, \boldsymbol{y}) \notin (-\infty, 0)$.
2. $q_\alpha(\boldsymbol{x}, \boldsymbol{y}) = 0 \Leftrightarrow \boldsymbol{x} = \boldsymbol{y}$.

Proof. We begin by writing q_α as

$$q_\alpha(\boldsymbol{x}, \boldsymbol{y})/R_\alpha^2 = r_x^{2/\hat{\alpha}(r_x)} + r_y^{2/\hat{\alpha}(r_y)} - 2r_x^{1/\hat{\alpha}(r_x)} r_y^{1/\hat{\alpha}(r_y)} \cos\theta_{xy}, \tag{B.1}$$

where $(r_x = |\boldsymbol{x} - \boldsymbol{x_c}|/R_\alpha, \theta_x)$ (resp. $(r_y = |\boldsymbol{y} - \boldsymbol{x_c}|/R_\alpha, \theta_y)$) are polar coordinates for $\boldsymbol{x}$ (resp. $\boldsymbol{y}$) centered at the corner $\boldsymbol{x_c}$, $\theta_{xy} = \theta_x - \theta_y$, and the scaling function $\hat{\alpha}$ satisfies $\hat{\alpha}(r) = \alpha$ if $r < 1$ and 1 if $r > 1$. The proof of both claims boils down to distinguishing cases.

1. Assume $(\boldsymbol{x}, \boldsymbol{y}) \notin B_\alpha^2$. We distinguish three cases.
   (i) If $\boldsymbol{x} \notin B_\alpha$ and $\boldsymbol{y} \notin B_\alpha$, i.e. $r_x \geq 1$ and $r_y \geq 1$, then $q_\alpha(\boldsymbol{x}, \boldsymbol{y}) \in \mathbb{R}$ satisfies

   $$q_\alpha(\boldsymbol{x}, \boldsymbol{y})/R_\alpha^2 = r_x^2 + r_y^2 - 2r_x r_y \cos\theta_{xy} \geq (r_x - r_y)^2. \tag{B.2}$$

   (ii) If $x \in B_\alpha$ and $\boldsymbol{y} \notin B_\alpha$, then

   $$q_\alpha(\boldsymbol{x}, \boldsymbol{y})/R_\alpha^2 = r_x^{2/\alpha} + r_y^2 - 2r_x^{1/\alpha} r_y \cos\theta_{xy}.$$

   Let us assume that $q_\alpha \in \mathbb{R}$. Since $\Im(q_\alpha)/R_\alpha^2 = 2\Im[r_x^{1/\alpha}]\left(\Re[r_x^{1/\alpha}] - r_y \cos\theta_{xy}\right)$, there are only two possible expressions

   $$q_\alpha(\boldsymbol{x}, \boldsymbol{y})/R_\alpha^2 = \begin{cases} r_y^2 - r_x^{\Re(2/\alpha)} & (\text{if } \Re[r_x^{1/\alpha}] = r_y \cos\theta_{xy}) \\ \left(\Re[r_x^{1/\alpha}] - r_y \cos\theta_{xy}\right)^2 + \left(r_y \sin\theta_{xy}\right)^2 & (\text{if } \Im[r_x^{1/\alpha}] = 0), \end{cases} \tag{B.3}$$

   which are both nonnegative. (iii) The case $\boldsymbol{x} \notin B_\alpha$ and $\boldsymbol{y} \in B_\alpha$ is identical to (ii) since $\boldsymbol{x}$ and $\boldsymbol{y}$ play a symmetric role.
2. If $\boldsymbol{x} = \boldsymbol{y}$, then $q_\alpha(\boldsymbol{x}, \boldsymbol{y}) = 0$. Conversely, assume that $(\boldsymbol{x}, \boldsymbol{y}) \notin B_\alpha^2$ and $q_\alpha(\boldsymbol{x}, \boldsymbol{y}) = 0$. We show that $\boldsymbol{x} = \boldsymbol{y}$ by distinguishing the same cases as above: (i) follows from (B.2), (ii) follows from (B.3), (iii) follows from (ii) by swapping $\boldsymbol{x}$ and $\boldsymbol{y}$.

□

Lemma 33. *Let $\Re(\alpha) > 0$ and $(\boldsymbol{x}, \boldsymbol{y}) \in \mathbb{R}^4$. If $|\boldsymbol{y} - \boldsymbol{x_c}| \leq |\boldsymbol{x} - \boldsymbol{x_c}|$ and $\boldsymbol{x} \neq \boldsymbol{x_c}$ we have*

1. $\hat{q}_\alpha(\boldsymbol{x}, \boldsymbol{y}) \notin (-\infty, 0)$.
2. $\hat{q}_\alpha(\boldsymbol{x}, \boldsymbol{y}) = 0 \Leftrightarrow \boldsymbol{x} = \boldsymbol{y}$.

3. *If* $\boldsymbol{x} \in \partial B_\alpha$, *then* $\hat{q}_\alpha(\boldsymbol{x}, \boldsymbol{y}) = q_\alpha(\boldsymbol{x}, \boldsymbol{y})$.

Proof. Let $\Re(\alpha) > 0$ and $(\boldsymbol{x}, \boldsymbol{y}) \in \mathbb{R}^4$. We assume that $r_x \geq r_y$ and $r_x \neq 0$, using the notation $(r_x, r_y, \theta_{xy}, \hat{\alpha}(r))$ introduced in the beginning of the proof of Lemma 32. Using (B.1) we can write $\hat{q}_\alpha$ as

$$\hat{q}_\alpha(\boldsymbol{x}, \boldsymbol{y})/R_\alpha^2 = 1 + \delta^2 - 2\delta \cos\theta_{xy}, \tag{B.4}$$

where for concision we denote $\delta = r_y^{1/\hat{\alpha}(r_y)} r_x^{-1/\hat{\alpha}(r_x)}$, a complex ratio that satisfies

$$|\delta| \geq 1 \text{ and } \left(|\delta| = 1 \Leftrightarrow r_x = r_y\right). \tag{B.5}$$

Before tackling each claim, let us state:

$$\Re(\hat{q}_\alpha(\boldsymbol{x}, \boldsymbol{y}))/R_\alpha^2 = 1 - \Im(\delta)^2 + \Re(\delta)\left[\Re(\delta) - 2\cos\theta_{xy}\right] \tag{B.6}$$

$$\Im(\hat{q}_\alpha(\boldsymbol{x}, \boldsymbol{y}))/R_\alpha^2 = 2\Im(\delta)\left[\Re(\delta) - \cos\theta_{xy}\right]. \tag{B.7}$$

1. Assume $\hat{q}_\alpha(\boldsymbol{x}, \boldsymbol{y}) \in \mathbb{R}$. From (B.7) we see that there are only two cases:

$$\hat{q}_\alpha(\boldsymbol{x}, \boldsymbol{y})/R_\alpha^2 = \begin{cases} 1 - |\delta|^2 \geq 0 & (\text{if } \Re[\delta] = \cos\theta_{xy}) \\ 1 + \delta^2 - 2\delta\cos(\theta_{xy}) \geq 1 - (\cos\theta_{xy})^2 & (\text{if } \Im[\delta] = 0), \end{cases} \tag{B.8}$$

   where the inequalities follow from (B.5) and Young's inequality.
2. If $\boldsymbol{x} = \boldsymbol{y}$, then from (B.4) we deduce $\hat{q}_\alpha(\boldsymbol{x}, \boldsymbol{y}) = 0$. Conversely, assume that $\hat{q}_\alpha(\boldsymbol{x}, \boldsymbol{y}) = 0$, so that (B.8) holds. (a) If $\Re(\delta) = \cos\theta_{xy}$, then $|\delta| = 1$ so that from (B.5) we have $r_x = r_y$, implying $\cos\theta_{xy} = 1$. (b) If $\Im(\delta) = 0$, then (B.6) is $0 = (\Re[\delta] - \cos\theta_{xy})^2 + (\sin\theta_{xy})^2$, hence $\sin\theta_{xy} = 0$ and $\Re(\delta) = \cos\theta_{xy}$, and we conclude as in case (a).
3. If $r_x = 1$, then $\delta = r_y^{1/\hat{\alpha}(r_y)}$ so that (B.1) and (B.4) are identical.

□

B.2. Complex scaling matrix

This section proves identities involving the product $J_\alpha A_\alpha$, which appears in e.g. the conormal derivative of the complex-scaled Green's function. We begin with the basic identities satisfied by the projection matrix P_c that appears in the definition of both A_α and J_α.

Lemma 34. *For any* $\boldsymbol{x} \neq \boldsymbol{x_c}$ *and* $\boldsymbol{y} \in \mathbb{R}^2$, *the projection matrix* $P_c(\boldsymbol{x})$ *given by* (23) *satisfies* $P_c(\boldsymbol{x})^2 = P_c(\boldsymbol{x})$, $P_c(\boldsymbol{x})(\boldsymbol{x} - \boldsymbol{x_c}) = \boldsymbol{x} - \boldsymbol{x_c}$, *and* $P_c(\boldsymbol{x})\boldsymbol{y} = \frac{(\boldsymbol{x}-\boldsymbol{x_c})\cdot\boldsymbol{y}}{|\boldsymbol{x}-\boldsymbol{x_c}|^2}(\boldsymbol{x} - \boldsymbol{x_c})$.

Using this result, we can obtain the following simplified expression.

Lemma 35. *Let* $\alpha \in \mathbb{C}^*$. *For any* $x \notin [\{\boldsymbol{x_c}\} \cup \partial B_\alpha]$,

$$J_\alpha(\boldsymbol{x}) A_\alpha(\boldsymbol{x}) = \frac{\mu_\alpha(\boldsymbol{x})}{\hat{\alpha}(\boldsymbol{x})}\left[I + (\hat{\alpha}(\boldsymbol{x}) - 1)P_c(\boldsymbol{x})\right]. \tag{B.9}$$

Proof. Compute the product of (22) and (25) and use Lemma 34. □

The next results focus on simplifying $A_\alpha J_\alpha \nu$ where ν is a unit normal vector.

Lemma 36. *Let $\alpha \in \mathbb{C}^*$. For any $x \notin [\{\boldsymbol{x_c}\} \cup \partial B_\alpha]$,*

$$J_\alpha(\boldsymbol{x})A_\alpha(\boldsymbol{x})(\boldsymbol{x}-\boldsymbol{x_c}) = \mu_\alpha(\boldsymbol{x})(\boldsymbol{x}-\boldsymbol{x}_c).$$

Proof. Follows from Lemmas 34 and 35. □

Lemma 37. *Let $\alpha \in \mathbb{C}^*$. For any $\boldsymbol{x} \in \partial B_\alpha$,*

$$\lim_{h\to\pm 0} J_\alpha(\boldsymbol{x}+h\boldsymbol{\nu}(\boldsymbol{x}))A_\alpha(\boldsymbol{x}+h\boldsymbol{\nu}(\boldsymbol{x}))\boldsymbol{\nu}(\boldsymbol{x}) = \boldsymbol{\nu}(\boldsymbol{x}), \tag{B.10}$$

where $\boldsymbol{\nu}$ is a unit normal vector.

Proof. Let $\boldsymbol{x} \in \partial B_\alpha$. Without loss of generality, we can choose $\boldsymbol{\nu}(\boldsymbol{x}) = (\boldsymbol{x}-\boldsymbol{x_c})/|\boldsymbol{x}-\boldsymbol{x_c}|$ as unit normal vector. By denoting $\boldsymbol{x}_h = \boldsymbol{x} + h\boldsymbol{\nu}(\boldsymbol{x})$ for concision, we have

$$\begin{aligned} J_\alpha(\boldsymbol{x}_h)A_\alpha(\boldsymbol{x}_h)\boldsymbol{\nu}(\boldsymbol{x}) &= J_\alpha(\boldsymbol{x}_h)A_\alpha(\boldsymbol{x}_h)\frac{\boldsymbol{x}_h-\boldsymbol{x_c}}{|\boldsymbol{x}-\boldsymbol{x_c}|} - hJ_\alpha(\boldsymbol{x}_h)A_\alpha(\boldsymbol{x}_h)\frac{\boldsymbol{\nu}(\boldsymbol{x})}{|\boldsymbol{x}-\boldsymbol{x_c}|} \\ &= \mu_\alpha(\boldsymbol{x}_h)\frac{\boldsymbol{x}_h-\boldsymbol{x}}{|\boldsymbol{x}-\boldsymbol{x_c}|} - hJ_\alpha(\boldsymbol{x}_h)A_\alpha(\boldsymbol{x}_h)\frac{\boldsymbol{\nu}(\boldsymbol{x})}{|\boldsymbol{x}-\boldsymbol{x_c}|}, \end{aligned}$$

where since $\boldsymbol{x}_h \notin \partial B_\alpha$ we used Lemma 36. Passing to the limit yields the claim. □

B.3. Gradient of the complex-scaled Green's function

In this section with gather statements involving the gradient of G_α.

Lemma 38. *Let $\Re(\alpha) > 0$. For any $\boldsymbol{y} \in \mathbb{R}^2$, we have*

$$f : \boldsymbol{x} \mapsto J_\alpha(\boldsymbol{x})\frac{\Gamma_\alpha(\boldsymbol{x})-\Gamma_\alpha(\boldsymbol{y})}{q_\alpha(\boldsymbol{x},\boldsymbol{y})} \in L^1_{\mathrm{loc}}(\mathbb{R}^2).$$

Proof. Let $\boldsymbol{y} \in \mathbb{R}^2$. From Lemma 11, $f \in C^0(\mathbb{R}^2\backslash[\{\boldsymbol{x_c},\boldsymbol{y}\} \cup \partial B_\alpha])$, so that it remains to verify that all the possible singularities are integrable. (i: $\boldsymbol{x} \to \partial B_\alpha\backslash\{\boldsymbol{y}\}$) From (22), we deduce that the singularity of f on ∂B_α is a jump discontinuity given by:

$$\forall \boldsymbol{x} \in \partial B_\alpha\backslash\{\boldsymbol{y}\},\ [\![f(\boldsymbol{x})]\!]_{\partial B_\alpha} = [\![1/\hat{\alpha}(\boldsymbol{x})]\!]_{\partial B_\alpha} P_c(\boldsymbol{x})\frac{\Gamma_\alpha(\boldsymbol{x})-\Gamma_\alpha(\boldsymbol{y})}{q_\alpha(\boldsymbol{x},\boldsymbol{y})}.$$

(ii: $\boldsymbol{x} \to \boldsymbol{x_c}$ and $\boldsymbol{y} \neq \boldsymbol{x}_c$) From the continuity of Γ_α at $\boldsymbol{x_c}$, we have

$$\frac{\Gamma_\alpha(\boldsymbol{x})-\Gamma_\alpha(\boldsymbol{y})}{q_\alpha(\boldsymbol{x},\boldsymbol{y})} \underset{\boldsymbol{x}\to\boldsymbol{x_c}}{\to} \frac{\boldsymbol{x_c}-\Gamma_\alpha(\boldsymbol{y})}{q_\alpha(\boldsymbol{x_c},y)} = \frac{\boldsymbol{x_c}-\boldsymbol{y}}{\mu_\alpha(\boldsymbol{y})|\boldsymbol{x_c}-\boldsymbol{y}|^2},$$

from which we deduce that $f(\boldsymbol{x}) \underset{\boldsymbol{x}\to\boldsymbol{x_c}}{=} O(\mu_\alpha(\boldsymbol{x})) \underset{\boldsymbol{x}\to\boldsymbol{x_c}}{=} O\left(|\boldsymbol{x}-\boldsymbol{x_c}|^{\Re(1/\alpha)-1}\right)$, which is integrable in $\mathbb{R}^2$ since $\Re(1/\alpha) > 0$ by assumption. (iii: $\boldsymbol{x} \to \boldsymbol{x_c}$ and $\boldsymbol{y} = \boldsymbol{x_c}$) From the definition of Γ_α:

$$f(\boldsymbol{x}) = J_\alpha(\boldsymbol{x})\frac{\boldsymbol{x}-\boldsymbol{x_c}}{\mu_\alpha(\boldsymbol{x})|\boldsymbol{x}-\boldsymbol{x_c}|^2} = \frac{1}{\hat{\alpha}(\boldsymbol{x})}\frac{\boldsymbol{x}-\boldsymbol{x_c}}{|\boldsymbol{x}-\boldsymbol{x_c}|^2} \underset{\boldsymbol{x}\to\boldsymbol{x_c}}{=} O\left(|\boldsymbol{x}-\boldsymbol{x_c}|^{-1}\right).$$

(iv: $\boldsymbol{x} \to \boldsymbol{y}$) The case $\boldsymbol{y} = \boldsymbol{x_c}$ is covered by (iii), so that we assume $\boldsymbol{y} \neq \boldsymbol{x_c}$. Since Γ_α is Lipschitz in a neighborhood of $\boldsymbol{y}$, $\Gamma_\alpha(\boldsymbol{x})-\Gamma_\alpha(\boldsymbol{y}) \underset{\boldsymbol{x}\to\boldsymbol{y}}{=} O(|\boldsymbol{x}-\boldsymbol{y}|)$, thus $f(\boldsymbol{x}) \underset{\boldsymbol{x}\to\boldsymbol{y}}{=} O\left(|\boldsymbol{x}-\boldsymbol{y}|^{-1}\right)$. □

Lemma 39. *Let $\Re(\alpha) > 0$. For any $\boldsymbol{y} \in \mathbb{R}^2 \backslash \{\boldsymbol{x_c}\}$ and $\varphi \in C_c^\infty(\mathbb{R}^2)$,*

$$\lim_{\varepsilon \to 0} \int_{\partial B(\boldsymbol{x_c}, \varepsilon)} \left[A_\alpha(\boldsymbol{x}) J_\alpha(\boldsymbol{x}) \frac{\Gamma_\alpha(\boldsymbol{x}) - \Gamma_\alpha(\boldsymbol{y})}{q_\alpha(\boldsymbol{x}, \boldsymbol{y})} \right] \cdot \boldsymbol{\nu}(\boldsymbol{x}) \varphi(\boldsymbol{x}) \, \mathrm{d}s(\boldsymbol{x}) = 0.$$

Proof. Using $A_\alpha = A_\alpha^T$, $J_\alpha = J_\alpha^T$, and Lemma 36, we can rewrite the integral as

$$I(\varepsilon) = \int_{\partial B(\boldsymbol{x_c}, \varepsilon)} \frac{\Gamma_\alpha(\boldsymbol{x}) - \Gamma_\alpha(\boldsymbol{y})}{q_\alpha(\boldsymbol{x}, \boldsymbol{y})} \cdot \boldsymbol{\nu}(\boldsymbol{x}) \mu_\alpha(\boldsymbol{x}) \varphi(\boldsymbol{x}) \, \mathrm{d}s(\boldsymbol{x}).$$

For ε small enough, $\boldsymbol{y} \notin B(\boldsymbol{x_c}, \varepsilon)$, so that using (21) we have the estimate

$$|I(\varepsilon)| \leq \left(\frac{\varepsilon}{R_\alpha} \right)^{\Re(1/\alpha)-1} \sup_{\boldsymbol{x} \in B(\boldsymbol{x_c}, \varepsilon)} \frac{|\varphi(\boldsymbol{x})|}{|\Gamma_\alpha(\boldsymbol{x}) - \Gamma_\alpha(\boldsymbol{y})|} \times 2\pi\varepsilon,$$

from which we deduce the claim since by assumption $\Re(1/\alpha) > 0$. □

Lemma 40. *Let $\Re(\alpha) > 0$, $\boldsymbol{y} \in B_\alpha \backslash \{\boldsymbol{x_c}\}$, and $\boldsymbol{x}_\varepsilon = \boldsymbol{y} + \varepsilon \hat{\boldsymbol{e}}_{\boldsymbol{r}}(\theta)$ where $\hat{\boldsymbol{e}}_{\boldsymbol{r}}(\theta) = [\cos\theta, \sin\theta]$. We have*

$$\lim_{\varepsilon \to 0} \frac{\Gamma_\alpha(\boldsymbol{x}_\varepsilon) - \Gamma_\alpha(\boldsymbol{y})}{q_\alpha(\boldsymbol{x}_\varepsilon, \boldsymbol{y})} \cdot [J_\alpha(\boldsymbol{x}_\varepsilon) A_\alpha(\boldsymbol{x}_\varepsilon)(\boldsymbol{x}_\varepsilon - \boldsymbol{y})] = \frac{1/\alpha}{1 + \left(\frac{1}{\alpha^2} - 1\right)(\cos(\theta - \theta_c))^2},$$

where θ_c is the polar angle of $\boldsymbol{x_c} - \boldsymbol{y}$.

Proof. We assume that ε is small enough so that $\boldsymbol{x}_\varepsilon \neq \boldsymbol{x_c}$. Since Γ_α is smooth around $\boldsymbol{y}$, Taylor-Young gives

$$\frac{\Gamma_\alpha(\boldsymbol{x}_\varepsilon) - \Gamma_\alpha(\boldsymbol{y})}{q_\alpha(\boldsymbol{x}_\varepsilon, \boldsymbol{y})} \underset{\varepsilon \to 0}{=} \frac{\varepsilon J_\alpha(\boldsymbol{y}) \hat{\boldsymbol{e}}_{\boldsymbol{r}} + O(\varepsilon^2)}{\varepsilon^2 [J_\alpha^2(\boldsymbol{y}) \hat{\boldsymbol{e}}_{\boldsymbol{r}}] \cdot \hat{\boldsymbol{e}}_{\boldsymbol{r}} + O(\varepsilon^3)}.$$

Combined with the continuity of $J_\alpha A_\alpha$ at $\boldsymbol{y}$, we deduce

$$\lim_{\varepsilon \to 0} \frac{\Gamma_\alpha(\boldsymbol{x}_\varepsilon) - \Gamma_\alpha(\boldsymbol{y})}{q_\alpha(\boldsymbol{x}_\varepsilon, \boldsymbol{y})} \cdot [J_\alpha(\boldsymbol{x}_\varepsilon) A_\alpha(x_\varepsilon)(\boldsymbol{x}_\varepsilon - \boldsymbol{y})] = \frac{[A_\alpha(\boldsymbol{y}) J_\alpha^2(\boldsymbol{y}) \hat{\boldsymbol{e}}_{\boldsymbol{r}}] \cdot \hat{\boldsymbol{e}}_{\boldsymbol{r}}}{[J_\alpha^2(\boldsymbol{y}) \hat{\boldsymbol{e}}_{\boldsymbol{r}}] \cdot \hat{\boldsymbol{e}}_{\boldsymbol{r}}}.$$

The claim then follows from the two algebraic identities (obtained using Lemma 34):

$$A_\alpha(\boldsymbol{y}) J_\alpha(\boldsymbol{y})^2 = \frac{\mu_\alpha(\boldsymbol{y})^2}{\alpha} I, \; J_\alpha^2(\boldsymbol{y}) = \mu_\alpha^2(\boldsymbol{y}) \left[I + \left(\frac{1}{\alpha^2} - 1 \right) P_c(\boldsymbol{y}) \right].$$

□

Lemma 41. *For any $\alpha \in \mathbb{C}$ such that $\Re(\alpha) > 0$,*

$$\frac{1}{2\pi} \int_{-\pi}^{\pi} \frac{1}{\alpha^2 (\cos\theta)^2 + (\sin\theta)^2} \, \mathrm{d}\theta = \frac{1}{\alpha}.$$

Proof. Proved using a contour integral in [13, App. A]. □

Lemma 42. *Let $\Re(\alpha) > 0$. For any $\boldsymbol{y} \in \mathbb{R}^2$ and $\varphi \in C_c^\infty(\mathbb{R}^2)$,*

$$\lim_{\varepsilon \to 0} \int_{\partial B(\boldsymbol{y}, \varepsilon)} \left[A_\alpha(\boldsymbol{x}) J_\alpha(\boldsymbol{x}) \frac{\Gamma_\alpha(\boldsymbol{x}) - \Gamma_\alpha(\boldsymbol{y})}{q_\alpha(\boldsymbol{x}, \boldsymbol{y})} \right] \cdot \boldsymbol{\nu}(\boldsymbol{x}) \varphi(\boldsymbol{x}) \, \mathrm{d}s(\boldsymbol{x}) = 2\pi \varphi(\boldsymbol{y}).$$

Proof. Using $A_\alpha = A_\alpha^T$ and $J_\alpha = J_\alpha^T$, we can rewrite the integral as

$$I(\varepsilon) = \int_{\partial B(\boldsymbol{y},\varepsilon)} \frac{\Gamma_\alpha(\boldsymbol{x}) - \Gamma_\alpha(\boldsymbol{y})}{q_\alpha(\boldsymbol{x},\boldsymbol{y})} \cdot [J_\alpha(\boldsymbol{x}) A_\alpha(\boldsymbol{x}) \boldsymbol{\nu}(\boldsymbol{x})] \varphi(\boldsymbol{x}) \, \mathrm{d}s(\boldsymbol{x}).$$

We distinguish cases on $\boldsymbol{y}$. (i) If $\boldsymbol{y} = \boldsymbol{x_c}$, using Lemma 36 we see that the integral is

$$I(\varepsilon) = \int_{\partial B(\boldsymbol{x_c},\varepsilon)} \frac{\Gamma_\alpha(\boldsymbol{x}) - \Gamma_\alpha(\boldsymbol{x_c})}{q_\alpha(\boldsymbol{x},\boldsymbol{x_c})} \cdot \boldsymbol{\nu}(\boldsymbol{x}) \mu_\alpha(\boldsymbol{x}) \varphi(\boldsymbol{x}) \, \mathrm{d}s(\boldsymbol{x}),$$

so that using $\Gamma_\alpha(\boldsymbol{x_c}) = \boldsymbol{x_c}$ we obtain

$$I(\varepsilon) = \int_{\partial B(\boldsymbol{x_c},\varepsilon)} \frac{\boldsymbol{x} - \boldsymbol{x_c}}{|\boldsymbol{x} - \boldsymbol{x_c}|^2} \cdot \boldsymbol{\nu}(\boldsymbol{x}) \varphi(\boldsymbol{x}) \, \mathrm{d}s(\boldsymbol{x}) \to 2\pi\varphi(\boldsymbol{x_c}).$$

(ii) If $\boldsymbol{y} \in \mathbb{R}^2_\alpha$, then $\Gamma_\alpha(\boldsymbol{x}) = \boldsymbol{x}$, $\Gamma_\alpha(\boldsymbol{y}) = \boldsymbol{y}$, and $A_\alpha J_\alpha = I$ so that

$$I(\varepsilon) = \int_{\partial B(\boldsymbol{y},\varepsilon)} \frac{\boldsymbol{x} - y}{|\boldsymbol{x} - y|^2} \cdot \boldsymbol{\nu}(\boldsymbol{x}) \varphi(\boldsymbol{x}) \, \mathrm{d}s(\boldsymbol{x}) \to 2\pi\varphi(\boldsymbol{y}).$$

(iii) Assume $\boldsymbol{y} \in B_\alpha$. This case is more involved since $J_\alpha A_\alpha \nu$ is not aligned with ν, as in the previous cases. Using Lemma 40 we deduce

$$\lim_{\varepsilon \to 0} I(\varepsilon) = \varphi(\boldsymbol{y}) \int_{-\pi}^{\pi} \frac{1/\alpha}{1 + \left(\frac{1}{\alpha^2} - 1\right)(\cos(\theta - \theta_c))^2} \, \mathrm{d}\theta,$$

which is $2\pi\varphi(\boldsymbol{y})$ from Lemma 41. (iv) When $\boldsymbol{y} \in \partial B_\alpha$, we split the circle integral along the boundary of the scaling region:

$$I(\varepsilon) = \left(\int_{\partial B(\boldsymbol{y},\varepsilon) \cap B_\alpha} + \int_{\partial B(\boldsymbol{y},\varepsilon) \setminus \overline{B_\alpha}} \right) \frac{\Gamma_\alpha(\boldsymbol{x}) - \Gamma_\alpha(\boldsymbol{y})}{q_\alpha(\boldsymbol{x},\boldsymbol{y})} \cdot [J_\alpha(\boldsymbol{x}) A_\alpha(\boldsymbol{x}) \boldsymbol{\nu}(\boldsymbol{x})] \varphi(\boldsymbol{x}) \, \mathrm{d}s(\boldsymbol{x}).$$

Each integral is dealt with as in cases (ii) and (iii), leading to

$$\begin{aligned} \lim_{\varepsilon \to 0} I(\varepsilon) &= \varphi(\boldsymbol{y}) \left[\left(\int_{-\pi}^{-\pi/2} + \int_{\pi/2}^{\pi} \right) \frac{1/\alpha}{1 + \left(\frac{1}{\alpha^2} - 1\right)(\cos\theta)^2} \, \mathrm{d}\theta + \int_{-\pi/2}^{\pi/2} \mathrm{d}\theta \right] \\ &= \varphi(\boldsymbol{y}) \left[\pi + \pi\right]. \end{aligned}$$

□